Tailorable metal–organic framework based thin film nanocomposite membrane for lithium recovery from wasted batteries

Bo Han, Sarah Chevrier, Qingyu Yan, Jean-Christophe Gabriel

Tailorable metal-organic framework based thin film nanocomposite membrane for lithium recovery from wasted batteries

Bo Han [1*], Sarah M. Chevrier [1,2], Qingyu Yan[1,3], Jean-Christophe P. Gabriel [1,2,*]

[1] SCARCE Laboratory, Energy Research Institute @ NTU (ERI@N),

Nanyang Technological University, Singapore 637459, Singapore

[2] LICSEN, NIMBE, CNRS, CEA, Université Paris-Saclay, 91191 Gif-sur-Yvette, France

[3]School of Materials Science and Engineering,

Nanyang Technological University, 639798, Singapore

* Correspondence: han.bo@ntu.edu.sg, jean-christophe.gabriel@cea.fr

Keywords: Lithium recovery, MIL-101 (Cr), Ionic liquid, TFN membrane, Nanofiltration

Abstract

This paper presents a tailorable method for the preparation of hierarchically structured membranes for efficient lithium recovery. Firstly, a metal-organic framework (MOF), namely MIL-101 (Cr), is grafted with different ionic liquids (ILs) onto its coordinate unsaturated site (CUS). The modified MOF (IL-MOF) is then used as nanoparticles to fabricate the hydrophilic polyvinylidene fluoride (PVDF) based thin film nanocomposite (TFN) membrane. Secondly, comprehensive characterizations of both the nanoparticle and the IL-MOF based TFN membrane are carried out. Thirdly, lithium recovery is performed experimentally using simulated lithium-ion batteries (LIBs) leaching solution with the as-synthesized membrane. The first order ageing test of TFN membrane is conducted by MOF detachment tendency investigation and ILs leaching tendency evaluation. The results show that IL-MOF nanoparticles have a significant effect on lithium recovery. Compared with the original membrane, the IL-MOF-TFN membrane exhibits a fourfold lithium selectivity enhancement for $S_{Li^+, Mn^{2+}}$ (from 1.73 to 8.91), $S_{Li^+, Co^{2+}}$ (from 1.75 to 9.94) and $S_{Li^+, Ni^{2+}}$ (from 1.69 to 10.09), as well as improved regeneration behavior, permeability (up to 45.0 L/(m^2·h·bar)) and

antifouling performance (flux recovery rate FRR up to 96.39%). It is found that 98.9% of the lithium was recovered from the feed solution over five repeated filtration cycles with maintained membrane integrity. This work highlights the advances in the design, modification and integration of MOFs into mechanically and chemically stable membrane technology for lithium recovery.

1. Introduction

Lithium is a strategic metal that is key to many applications, such as glass, ceramics and polymer production, lubricants and battery technologies [1]. The lithium market is already under pressure as lithium-ion batteries (LIBs) are the most widely used rechargeable batteries in many electronic products, such as portable computers, electric vehicles, and mobile phones. This market is further stressed by the centralization of production in only a few mines and the 6% annual increase in consumption reported over the last decade [2]. Over-consumption, price increases and improper disposal of lithium compounds are leading to lithium scarcity and environmental pollution [3, 4], making it necessary to develop efficient recycling processes. In general, industrial lithium extraction is mainly achieved by lithium recovery from aqueous resources such as salt-lake brine and spent lithium-ion batteries (LIBs) leach liquor, due to its higher reserves and lower cost [2]. It should be noted that the conventional precipitation method is not applicable for lithium recovery when low amounts of lithium (in terms of mass ratio) are present in the feed solution [5, 6]. Other Li recovery approaches such as lithium ion-sieve (LIS) [7] and solvent extraction [8] result in large amounts of wastewater. In addition, LIS and solvent extraction require multiple steps such as adsorption/desorption and extraction/stripping, respectively. These shortcomings add to the complexity of lithium recovery. In the recent decades, many researchers have proved that membrane technology-based lithium recovery process such as ion-imprinted membrane [9], supported liquid membrane [10], electrodialysis [11] and membrane distillation crystallization [12] is less energy intensive, environmentally

friendly and does not change the state of lithium. Therefore, research on membrane technology for lithium recovery is of industrial and environmental importance. Among all the membrane-based technologies, nanofiltration (NF) membrane has been widely used for the separation of low molecular weight organics and divalent ions from aqueous environments due to its relatively high selectivity [13]. It should be noted that NF is the only membrane technology for large-scale lithium recovery applications [2]. The main separation mechanisms of NF membranes are steric exclusion and electrostatic effect [14, 15]. However, NF membranes have an unavoidable trade-off defect: a high solvent permeability is accompanied by a low solute selectivity and *vice versa*. The trade-off defect of NF membranes has hindered their further industrial and commercial development. In addition, problems such as non-selective interfacial voids, poor dispersion and nanoparticle aggregation are common, resulting in poor separation performance.

Recently, the use of the thin film composite (TFC) membrane has gradually increased [16]. As an energy-efficient NF membrane [17], the TFC membrane consists of a porous support substrate and a thin polyamide film (ultrathin selective layer) [18, 19]. The typical configuration of TFC membranes could be subdivided into : 1) a top ultrathin skin polyamide (PA) layer which controls the separation performance; 2) a middle porous support layer which provides the necessary mechanical support and functions as a platform for IP process; and 3) a bottom nonwoven fabric layer which gives further mechanical support. The ultrathin selective layer is prepared by interfacial polymerization (IP) in situ on the surface of the porous support substrate. IP is a diffusion reaction process and mainly occurs between organic monomers (acyl chlorides) and aqueous diamine monomers, where the aromatic polyamide (PA) is formed at the oil-water interface as a result of polycondensation of acyl chlorides and diamines. The diffusion rate of IP can be well-controlled and highly permeable polyamide films is obtained by using advanced techniques such as low temperature reaction [20], macromolecule

incorporation [21], nano-foaming [22] and electro-spraying [23]. Typically, polyamide films formed by IP should have either an ultrathin layer with reduced mass transfer resistance or a robust surface with abundant free transport sites [24, 25]. Both of these characteristics result in improved water permeability. As for the polymer substrate, polyvinylidene fluoride (PVDF) membrane is always an attractive choice due to its promising chemical stability, excellent compatibility and high mechanical strength. However, the lack of unsaturated functional groups on the surface results in poor separation performance [26]. In addition, the foremost problems with the TFC membrane is its interfacial defects and low retention/poor selectivity of multivalent salts [27]. One way to overcome these problems is to incorporate nanomaterials into TFC membranes to form thin film nanocomposite (TFN) membranes. The embedded nanofillers create additional channels for the transfer of target molecules through their inherent interfacial voids and nanopores within the PA layer. This unique structure gives TFN membranes both outstanding solvent permeability and excellent solute selectivity. To date, various nanomaterials such as graphene oxide (GO) [28], carbon nanotubes (CNTs) [29], zeolite [30] and nanoclay [31] have been employed for the preparation of TFN membrane. Recently, metal-organic frameworks (MOFs) are attracting increasing attention as nanofillers. MOFs are crystalline porous materials composed of metal ions (or clusters) and organic ligands. Benefiting from the presence of organic ligands, MOFs show higher affinity/compatibility with polymer chains than inorganic porous nanomaterials such as zeolite [32]. Consequently, high affinity/compatibility leads to controllable MOFs-polymer interfacial interactions, which has a favorable effect on the formation of relatively ideal interfacial cavities, while solute rejection is largely maintained [32]. In addition, MOFs show superiority over other nanomaterials due to their versatile functional organic linkers, ordered porous cavities, high specific surface area and tailorable structures. The incorporation of porous MOFs with specific pore size could enhance the size exclusion effect of the TFN membrane, thus achieving high selectivity or

rejection rate of metal ions [33-35]. Besides that, additional water transfer pathways are usually created within the unique MOF channels, which brings favorable effect on the water permeance [36, 37]. In addition, the use of hydrophilic MOFs on the TFN membrane would also improve the surface wettability, which also leads to the higher water permeability [38, 39]. Therefore, the trade-off defect in NF membranes is addressed. Such phenomenon has also been reported in other works [40, 41]. Among all the MOFs, a chromium terephthalate-based MOF, namely MIL-101 (Cr) [42], has been considered as a potential candidate for TFN membrane technology. Structurally, MIL-101 (Cr) is a micro-mesoporous material with giant pore size (~ 30 to 34 Å), high pore volume (~ 702,000 $Å^3$) and large Langmuir surface area (~ 5900 $\pm$ 300 m^2/g). In addition, MIL-101 (Cr) is chemically stable in aqueous environments due to the strong coordination bonds between carboxylate-type linkers and high-valence metal ions Cr^{3+} [43]. One of the main advantages of MIL-101 (Cr) is that it has two mesoporous cages with internal free diameters of ~ 29 Å and 34 Å, respectively. These large openings always result in high solution flux. In a study, Sorribas et al. [32] used MIL-101 (Cr) based TFN membrane for organic solvent nanofiltration and an exceptional increase in permeance from 1.7 up to 11.1 $L \cdot m^{-2} \cdot h^{-1} \cdot bar^{-1}$ for tetrahydrofuran/styrene oligomer solution is observed. To date, although several works have reported the remarkable permeability of MIL-101 (Cr) based TFN membranes in organic solvent nanofiltration application, the study of MIL-101(Cr)-based TFN membranes used for metal ion separation has rarely been directly investigated. This is mainly due to the main characteristic of the original MIL-101 (Cr): oversized cages. In general, the large cavities in cage-type MOFs such as MIL-101 (Cr) are separated by smaller windows. During the ion separation process, the diffusion of the target ions through the cavities could be controlled by the size-sieving effect of the windows [44]. A competent MOF should have window sizes that allow target ions to pass and prevent larger non-target ions from passing [45]. Unfortunately, the smaller cages of the MIL-101 (Cr) have pentagonal windows with a

free aperture of ~ 12 Å, while the larger cages have both pentagonal and hexagonal windows with a free aperture of ~14.5 Å by 16 Å [42]. Compared to the size of the hydration diameter of many typical target ions (such as Li^+ 7.64 Å, Ni^{2+} 8.08 Å, Ca^{2+} 8.24 Å and Al^{3+} 9.60 Å), these large windows almost make the passage for all ions. This results in poor metal ion separation performance.

To overcome this drawback, modification on the parent MIL-101 (Cr) is required. Approaches such as organic ligand functionalization [14], nanocomposite fabrication [46], and temperature adjustment [47] have been applied for the controllable tuning of the porosity of MOFs, which will further modify the properties (such as hydro-stability, selectivity of different gases/ions) of MOFs. Beyond these methods, an alternative option to solve this problem is the encapsulation of ionic liquids (ILs). ILs encapsulation is a post-synthetic modification process, in which organic cations and organic/inorganic anions are encapsulated onto the CUS (coordinate unsaturated site) of MOFs. By encapsulating these ionic liquid guests onto the MOF framework, the CUS is occupied, the pore size distribution is tailored, the ion exchange property as well as the ionic conductivity is improved and the electrostatic repulsion between the target ions and the charged membrane surface is enhanced [45]. Nowadays, ILs encapsulation on MOFs (referred to as IL-MOFs) based membranes have been widely used in many applications, such as IL-MOF-5 membrane for biogas upgrading [48], IL-IRMOF-1 membrane for CO_2 capture [49], IL-ZIF-8 membrane for gas screening, and IL-UiO-66-NH_2 membrane for air-dehumidification [50]. However, no study has focused on the lithium recovery using IL-MOFs based TFN membranes. All these limitations mentioned above provide the motivation to propose one comprehensive study on IL-MOFs based TFN membranes, from MOFs modification, membrane fabrication, characterization to the lithium recovery performance evaluation. Based on the above introduction, the main objectives of this work include: (i) synthesis and modification (ILs encapsulation) on the original MIL-101 (Cr)

MOF; (ii) development of MIL-101 (Cr) based TFN membrane; (iii) characterization of the MOF particles and IL-MOF based TFN membranes; (iv) test the effect of ionic liquid on the performance of TFN membranes; and (v) evaluation on the lithium recovery performance in terms of water permeability, lithium selectivity, antifouling behavior and antiaging performance.

2. Experimental section

2.1 Materials and chemicals

Commercially available hydrophilic polyvinylidene fluoride (PVDF) substrate was purchased from Merck, all chemicals were of analytical grade and used without further purification. Chromic nitrate nonahydrate ($Cr(NO_3)_3 \cdot 9H_2O$, 99%), terephthalic acid (H_2BDC, C_6H_4-1,4-$(CO_2H)_2$, 98%, H_2BDC), ammonium fluoride (NH_4F, ≥ 98%), piperazine ($C_4H_{10}N_2$, 99%, PIP), 1,3,5-Benzenetricarbonyl Trichloride ($C_6H_3(COCl)_3$, 98%, TMC), dimethylformamide (DMF, 99.8%), ethanol (C_2H_5OH, ≥ 99.8%), concentrated hydrochloric acid (HCl, 37%), hexane ($CH_3(CH_2)_4CH_3$, ≥ 97%) and all the ionic liquids (ILs) were purchased from Merck. Collectively, all imidazolium-based ILs used in this work contained the identical cation of 1-Butyl-3-methylimidazolium $[BMIM]^+$, but had four different anions namely chloride $[Cl]^-$, bromide $[Br]^-$, tetrachloroaluminate $[AlCl_4]^-$, and methanesulfonate $[MeSO_3]^-$. Two 1-Ethyl-3-methylimidazolium $[EMIM]^+$ based ionic liquids with chloride $[Cl]^-$ or bromide $[Br]^-$ as anions were also used. The molecular structures of these ionic liquids are shown in Figure S1. All chemicals are of analytical grade and used without further purification. Furthermore, the feed solution components were simulated based on the real LIBs (NMC) leaching solution, which is furnished in Table S1.

2.2 MOF synthesis

Original MIL-101 (Cr)

Hydrothermal reaction method was used for the synthesis of original MIL-101 (Cr) [42]. Firstly, equimolar (0.01 mol) of chromic nitrate nonahydrate ($Cr(NO_3)_3 \cdot 9H_2O$), terephthalic acid (H_2BDC, C_6H_4-1,4-$(CO_2H)_2$) and concentrated HCl were mixed in 48 ml of deionized water. The mixture was stirred for 30 mins under ambient condition. Secondly, the mixture was transferred into the liner, tightly sealed in the Teflon-lined stainless-steel autoclave reactor, and heated under 220 °C for 16 h. Thirdly, the autoclave was cooled down naturally. The mixture was filtrated from the solution and crystalline green solid was obtained. It was noted that a certain amount of recrystallized or unreacted H_2BDC was trapped both inside/outside the pores of MIL-101 (Cr). These impurities always lead to a low yield and poor quality of the final product; therefore, rigorous purification procedures were needed. Initially, the mixture was filtered consecutively through the large pore fritted glass filter (no.2) and small pore (no.5) paper filter. Next, the green solid was eluted with hot dimethylformamide (DMF) and ethanol (three times). Finally, the as-synthesized MIL-101 (Cr) was dried at 80 °C overnight and activated at 160 °C for 5 h under vacuum conditions. The activation process was designed to remove water vapour, residual reagent and any other impurities.

Dehydration

1 g of activated MIL-101 (Cr) was immersed in 200 ml of ammonium fluoride (NH_4F, 1 M) and stirred at 80 °C for 24 h. This dehydration process aimed to create the coordinatively unsaturated chromium sites (CUS) at the secondary building unit (SBU) of the MIL-101 (Cr). The dehydrated MIL-101 (Cr) was directly washed with hot ethanol (3 x 50 ml) without cooling, dried at 80 °C overnight and vacuum-heated at 160 °C for 5 h.

Ionic liquid encapsulation

The wet-impregnation method was used to encapsulate the ionic liquids onto MIL-101 (Cr), typically using 1 g of activated dehydrated MIL-101 (Cr) and 1 g of 1-Butyl-3-Methylmidazolium chloride ($[BMIM]^+[Cl]^-$) dispersed in 100 ml of ethanol liquor. The mixture was stirred for 24 h at ambient pressure and temperature to encapsulate the ILs onto the CUS of the dehydrated MIL-101 (Cr). To make a better ILs encapsulation in the MOFs, the original MOFs are first dispersed in 50 ml of ethanol liquor and stirred for 15 min, and the ILs are dispersed in 50 ml of ethanol liquor and stirred for 15 min. Next, these two solutions are mixed together and stirred at 200 rpm (the stirring speed can neither be too slow nor too furious). The IL-MOFs sample was then filtrated, washed with ethanol (2 x 50 ml), dried at 80 °C overnight, and activated at 160 °C for 5 h, to obtain $[BMIM]^+[Cl]^-$ type ILs encapsulated MIL-101 (Cr) with an impregnation weight ratio of 1:1, nominalized as "1:1 [BMIM][Cl]-MIL-101 (Cr)". It is noted that the ILs encapsulation procedures remained the same for all the IL-MOFs materials, but with varying types and amounts of ILs.

2.3 MOF-TFN membranes fabrication

The development of MOF-TFN membranes involved four main steps: (i) solution preparation. Solution A: 100 ml aqueous solution containing 0.1% (w/v) original or modified MIL-101 (Cr), 0.2% (w/v) piperazine (PIP) and deionized water was prepared by sonication. Solution B: 100 ml of organic solution was prepared by dissolving 1,3,5-benzenetricarbonyl trichloride (0.15% (w/v)) in hexane; (ii) vacuum filtration. 10 ml of solution A was poured onto the vacuum filtration vessel and filtered through the PVDF substrate; (iii) interfacial polymerization (IP): 6 ml of solution B was added to the PIP-MOFs-embedded PVDF substrate for 1 min. Thus, the polyamide layer of the MOF-TFN membrane was obtained by interfacial polymerization of a PIP (piperazine)/MOF aqueous phase and a TMC (1,3,5-benzenetricarbonyl trichloride/trimesoyl chloride) organic phase; and (iv) thermal treatment. Excess organic liquids were removed, the membrane was heated at 70 °C for 5 min (annealing treatment). To

test the effect of the MOF loading amount, different amounts of MOF nanofillers were added to the PVDF substrate by varying the volume (5 ml, 10 ml and 15 ml) of solution A, and the as-prepared MOF-TFN membranes were designated as M5, M10 and M15, respectively.

2.4 Characterization

MIL-101 (Cr) based MOFs

The crystallographic structure of the MIL-101 (Cr) based MOFs was determined by X-ray diffraction (XRD). The microstructure, morphology and particle size of the MOFs were investigated by FESEM (Field Emission Scanning Electron Microscopy). The functional groups of the MOFs were tested by FTIR (Fourier Transform Infrared Spectroscopy) characterization. The thermal stability of the original and modified MOFs was tested by TGA (Thermal Gravimetric Analysis) and their charging properties were investigated by Zeta potential analysis. In addition, the N_2 adsorption/desorption experiment are conducted by ASAP Tri-star II 3020 at 77 K to determine the porosity of the MOFs. To remove any undesirable adsorbed vapours and water, the sample is outgassed at 160 ℃ for 3 h before N_2 adsorption experiment. The N_2 isotherms data can be deduced to calculate adsorbent-surface area by using BET (Brunuer-Emmet-Teller) equation. Total pore volume is obtained under saturation conditions ($P/P_s = 1$), which is equivalent to the total liquid N_2 adsorbed in the MOF sample. The liquid volume is calculated by $V_{liq} = \frac{P_a V_{ads} V_m}{RT}$, where P_a is the ambient pressure, V_{ads} is the volume of N_2 adsorbed, V_m is the molar volume of liquid of N_2 with a value of 3.47×10^{-5} m^3/mol, R defines the gas constant and *T* is the temperature. Moreover, the average pore size (r_p) is calculated by $r_p = \frac{2V_{liq}}{A_s}$, where A_s is the BET surface area of the adsorbent sample. In addition, the micropore volume is calculated as $V_{micropore}$ = (Y_{INT} cm^3/g *STP) x (D* cm^3 *liquid/*cm^3 *STP)*, where Y_{INT} is the Y-intercept obtained from the Langmuir surface area transformation model and *D* is the density conversion factor.

MOF-TFN membranes

The MOF additive layer as well as the chemical composition of the uppermost surface of the TFN membrane were verified by XPS (X-ray Photoelectron Spectroscopy). ATR-FTIR (attenuated total reflection-Fourier transform infrared) technique was used to determine the MOF-TFN membrane's functional groups for wavenumbers 4000 to 650 cm^{-1}. X-Ray Fluorescence Spectrometry was applied to determine the elemental composition (Cr) of the TFN membrane. The MOF-TFN membrane's surface morphology and thickness were measured by FESEM, its wettability (surface hydrophilicity) was tested via contact angle analysis, and its surface roughness was analyzed by AFM (atomic force microscopy) technique using a scan size of 10 µm × 10 µm under NCM (non-contact) mode.

2.5 Lithium recovery experiments

Metal ion separation

The metal ion separation experiments were carried out using the commercially available high pressure (HP4750) stirred cell apparatus from STERLITECH (Figure S2). In general, the IL-MOF enabled TFN membrane was placed on the porous stainless steel membrane support and fixed to the cell bottom. Feed solution (simulated LIBs leaching solution) was added to the cell body. After the whole apparatus was well sealed, dry nitrogen gas (99.999%, 2.5 to 15 bar) was supplied from the top of the cell. The feed solution was then flushed through the membrane, discharged through the permeate tube and collected in the beaker. During the experiment, the beaker was placed on the balance, which was connected to built-in weight-time analysis software. This automatically recorded the change in weight of the permeate solution as a function of time for further derivation of water flux and permeability. The concentration of metal ions in the permeate solution was measured by ICP (Inductively Coupled Plasma) analysis.

Regeneration and fouling test

Regeneration and fouling test: After the metal ion separation experiments, the used MOF-TFN membrane was placed in the deionized water and stirred at ambient conditions for regeneration purposes. During stirring in deionized water, the hydrodynamic shear stress generated by the stirring tends to detach the contaminants from the membrane surface as well as from the pores of the MOF. Therefore, the recovered membrane can then be used for the next cycle. Metal ion rejection experiment, water flux and permeability were compared after each regeneration cycle at 7.5 bar. The fouling performance of TFN membranes was mainly influenced by two factors, namely feed solution composition (type/concentration of foulant) and hydrodynamic operating conditions (such as cross-flow velocity). In this work, the fouling performance of the as-manufactured membrane was tested using BSA (bovine serum albumin, 200 mg/L) as a foulant in a multi-ion solution at 10 bar for 4 h continuously. The contaminated membrane was then repeatedly rinsed in water for 1 h.

Ageing test

The first order ageing test of TFN membrane was conducted in two ways: (i) the detachment tendency of nanoparticles was tested using a modified quantification method as reported by Ng et al. [51] and (ii) the leaching tendency of ionic liquids from MOFs was tested for four filtration cycles. For detachment tendency evaluation, IL-MOF-TFN membrane (M15) was placed in the deionized water (V_{H_2O} = 100 ml) and constantly stirred at the room temperature for 12 h. This procedure aimed to investigate the stability and adhesion of MOF nanoparticles within the TFN membranes. If the interaction was poor, hydrodynamic shear stress created from the agitation tends to detach MOF-based nanoparticles from the membrane. The concentration of chromium ions (C_{Cr}) in the solution was tested every 1 h by ICP analysis. Knowing that the weight percentage of Cr (Cr%) inside MIL-101 ($Cr_3O(OH)(H_2O)_2(bdc)_3$, bdc = benzene-1,4-dicarboxylate) is 21.74% and the total mass of MIL-101 nanoparticle (M_{MOF})

on M15 TFN membrane is 15 mg, the detachment percentage of MOF (D_{MOF} *(%)*) is calculated as

$$D_{MOF}\ (\%) = \frac{C_{Cr} \cdot V_{H_2O}}{Cr\% \cdot M_{MOF}} \times 100\% \quad (1)$$

In addition, for leaching tendency test of ionic liquids from MOFs, in each cycle, 250 ml of simulated LIBs leaching solution was purged through the membrane at the transmembrane pressure of 5 bar. The lithium concentration of the permeate solution was measured by ICP and the transmittance intensity of the IL-MOF-TFN membranes were evaluated by ATR-FTIR characterization before and after each filtration cycle. The area of each ATR-FTIR band has been calculated using OriginPro software between the ATR-FTIR profile and a baseline corresponding to the maximum transmittance.

2.6 Membrane performance evaluation

Separation factor (Selectivity, S_{M_1,M_2})

$$S_{M_1,M_2} = \frac{c_{M_1,p}/c_{M_2,p}}{c_{M_1,f}/c_{M_2,f}} \quad (2)$$

where $c_{M_1,p}$ and $c_{M_1,f}$ stand for the concentration of metal ion M_1 in the permeate and feed solution, respectively. $c_{M_2,p}$ and $c_{M_2,f}$ indicate the concentration of metal ion M_2 in the permeate and feed solution, respectively. Hence, $S_{M_1,M_2} = 1$ means that the membrane has no separation effect for M_1 and M_2 ions. On the other hand, $S_{M_1,M_2} > 1$ suggests that M_1 ions penetrate the membrane preferentially over M_2 ions [5].

Water flux (J_w, L/(m^2·h) or LMH)

$$J_w = \frac{\Delta V}{A_m \cdot \Delta t} \quad (3)$$

where ΔV is the changing volume of permeate solution (L), A_m denotes the effective membrane surface area (0.0009 m^2) and Δt stands for the permeation time (s) [52].

Water permeability (A, L/(m^2·h·bar))

$$A = \Delta V/(A_m \cdot \Delta t \cdot \Delta P) \quad (4)$$

where ΔV is the volume of permeate solution (L), A_m stands for the effective surface area of the membrane, Δt indicates the permeation time (s) and ΔP represents the system pressure (bar) [53].

Flux recovery rate (FRR, %)

$$FRR = (\frac{J_{w2}}{J_{w1}}) \times 100 \quad (5)$$

where J_{w1} is the initial water flux of the fresh membrane and J_{w2} is the subsequent water flux of the membrane after fouling [54].

3. Results and discussion

3.1 Characterization on MIL-101 (Cr) based MOFs

In this section, 2:1 [BMIM][$AlCl_4$]-MIL-101 (Cr) is selected as an example, other characterization results such as PXRD, FTIR, SEM, N_2 adsorption and TGA for all the ionic liquid modified MIL-101 (Cr) are elaborated in the supporting document (Figure S3, Figure S4, Figure S5, Table S2 and Figure S6, respectively). Figure 1(a) shows the PXRD (powder X-ray diffraction) profiles of the pristine MIL-101 (Cr) and IL-MOF. Based on the result, peaks appearing near 5.5°, 6.1°, 8.8°, 9.4°,10.7°, 16.9° and 18.9 ° agree with those reported in the literature [42], which proves that the original MOF is well developed. Similar XRD profiles are found between original and modified MOFs. Therefore, the structure integrity of the MIL-101 (Cr) nanoparticle is not distorted by the ionic liquid encapsulation work. The FTIR plots of the parent MIL-101 (Cr) and IL-MOF are shown in Figure 1(b). Peak at 577 cm^{-1} is ascribed to the Cr-O vibration. The band appearing near 749 cm^{-1} and 1117 cm^{-1} is related to the γ(C-H) and σ(C-H) vibrations of aromatic rings, respectively. Additionally, C=O group vibration is responsible for the band near 1635 cm^{-1}. Furthermore, due to the existence of dicarboxylate linker inside the MOF structure, band appearing at 1392 cm^{-1} corresponds to the symmetric (O-C-O) vibration. These FTIR peaks are consistent with those reported by other work [55, 56]. It is observed that besides the original distinct peaks, few extra peaks at certain wavenumber

are detected for the modified MIL-101 (Cr). This is mainly because of the new generated chemical bonding from the ionic liquid additives and MOF framework.

The morphology as well as the particle size of the original MIL-101 (Cr) are displayed in Figure 1(c.1), from where discrete octahedron with smooth surface is found. It is noted that some crystals with lack angles or split morphology are due to the fabrication defect and a few rod-like shape crystals are faulty MOF particles or recrystallized organic ligand [57]. It is found that the as compared with the parent MOF, IL-MOF exhibits similar octahedral shape with comparable size (Figure 1(c.2)). However, it should be noted that during the modification process, MOFs are hydrated with excessive NH_4F and vacuum-heated at relatively high temperature. Such activities may change/cleave the particle shapes and the morphologies of the original MOF. Therefore, some irregular crystal shapes can be observed in the IL encapsulated MOFs. The SEM images prove that the morphologies of the ionic liquid encapsulated MOF are maintained and the micro-structure of the original MIL-101 (Cr) is not destroyed by ionic liquid encapsulation. Furthermore, Figure 1(d) shows the nitrogen adsorption isotherm of MIL-101 (Cr) and the detailed porosity analysis is discussed in *3.3 Lithium recovery performance* section. Compared with the original MOF, a lower limiting adsorption amount of N_2 is found for the modified MOF, which is mainly due to the fact that the ionic liquid additives occupy a partial porous space. In addition, the TGA graph of the original MIL-101 (Cr) is shown in Figure 1(e), where a three-stage weight loss of the original MOF is observed as the temperature increases from 30 °C to 600 °C. Firstly, a 1.75% of weight loss between 30 °C to 85 °C is ascribed to the departure of water molecules from the outer cage of MOF. Secondly, more water vapor is dehydrated from the micropores as the temperature increases up to 500 °C. Majority of the weight loss (55.87%) is found during this process, the MOF framework collapses and decomposition near 350 °C is observed. Finally, material is carbonized at higher temperature (~ 600 °C) and around 35.52% weight residue is obtained. A similar weight loss

profile is observed for the IL-MOF, where a higher weight loss (8.72%, due to the high water affinity of the ionic liquids) is obtained in the first stage and a lower weight residue (28.05%, due to the removal of the ionic liquid at higher temperature) is obtained. These results demonstrate the successful encapsulation of the ionic liquid in the MIL-101 (Cr).

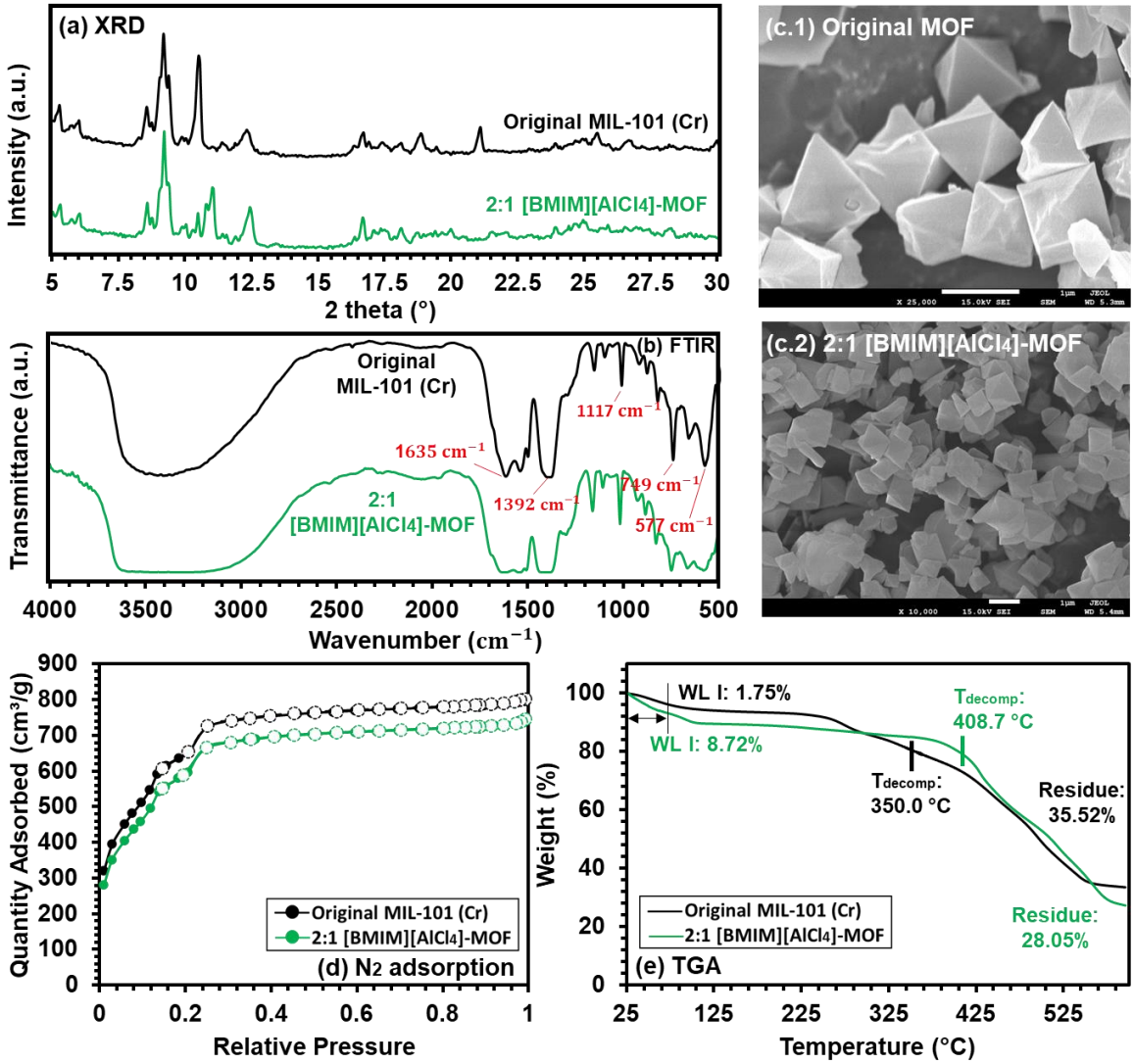

Figure 1: Characterization of original and IL encapsulated MIL-101 (Cr) MOF: (a) XRD, (b) FTIR, (c.1-c.2) SEM, (d) N_2 adsorption and (e) TGA profiles.

3.2 Characterization on MOF-TFN membranes

Chemical structures

The chemical structure of the pure PVDF substrate and MIL-101 (Cr) based MOFs incorporated TFN membrane skin layer is investigated by ATR-FTIR. For a pure PVDF substrate (Figure 2(a.1)), peaks found around 836 and 875 cm^{-1} correspond to the CF stretching vibration and the asymmetric C-C-C stretching vibration. An absorption peak near 1173 cm^{-1} is attributed to the C-C band. An absorption peak of CH_2 wagging vibration is observed near 1402 cm^{-1}. Bands showed at 1730 cm^{-1} and 1828 cm^{-1} are related to the C=C stretching vibration [58] and bands appearing around 2982 and 3024 cm^{-1} are attributed to the CH_2 symmetric and asymmetric vibration of PVDF substrate [59]. For the original MIL-101 (Cr) incorporated TFN membrane (Figure 2(a.2)), additional peaks are mainly attributed to the interfacial polymerization as well as the MOFs within the polyamide selective layer. New peaks appearing for the ILs encapsulated MOF incorporated TFN membrane correspond to the ILs additives within the MOF (Figure 2(a.3)). The detailed ATR-FTIR analysis is shown in Figure S7. The presence of new peaks compared to the original pure PVDF substrate indicates the efficient incorporation of MOFs into the membrane structure. The ATR-FTIR profiles for all membranes are provided in the supporting documents (Figure S8) for full understanding. Figure 2(b.1-b.3) shows the XRF curves for the three types of membranes. The main purpose of the XRF is to prove the successful loading of the Cr-based MOF onto the TFN membrane. For better comparison, three XRF profiles (pure PVDF, MOF-TFN membrane, and IL-MOF-TFN membrane) are plotted on a graph under the same y-axis (intensity) scale. Compared to the pure PVDF substrate (Figure 2(b.1)), the apparent peaks for both the original (Figure 2(b.2)) and modified (Figure 2(b.3)) MOF-based TFN membranes at 5.41 and 5.95 keV are attributed to the Cr-based MIL-101 (Cr) nanoparticles on the membrane surface.

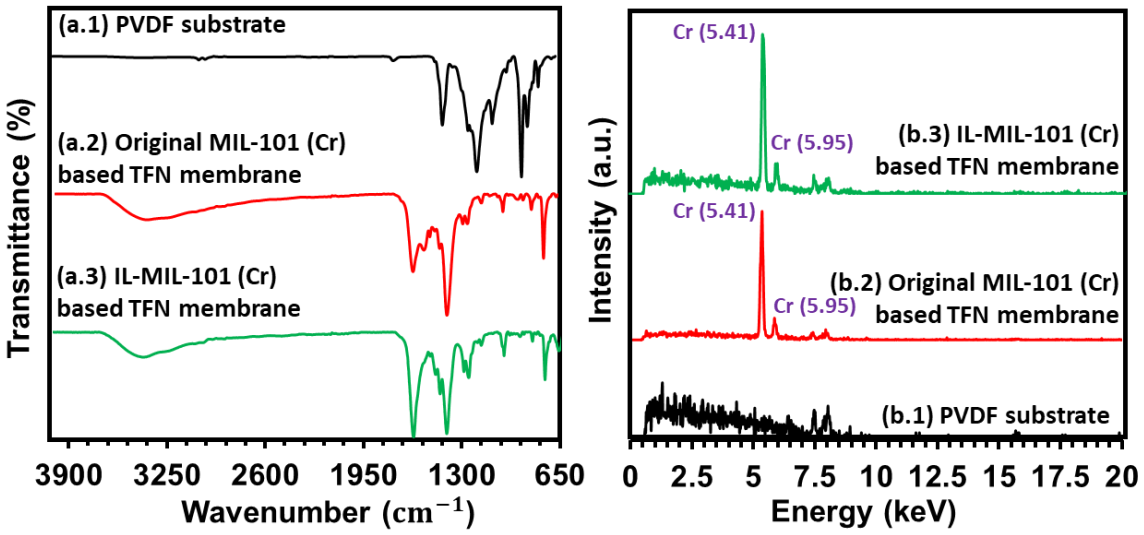

Figure 2: (a.1-.3) ATR-FTIR profiles and (b.1-b.3) XRF curves of pure PVDF substrate, MOF based TFN membrane and ILs encapsulated MOF based PVDF membrane.

In addition, Figure 3(a) shows the XPS wide-scan profiles for the pure PVDF substrate, the original MIL-101 (Cr) based TFN membrane and the IL-encapsulated MIL-101 (Cr) (IL-MOF) based TFN membrane. The detailed elemental composition analysis is shown in Figure 3(a.2) for oxygen (O), Figure 3(a.3) for nitrogen (N) and Figure 3(b.1-b.3) for carbon (C). For example, as shown in Figure 3(b.1), five Gaussian peaks at 285.9 eV, 286.8 eV, 288.6 eV, 290.5 eV and 291.3 eV of the C1s core electron spectrum are attributed to C-C/C-H, CH_2, C-O (adventitious carbon), C=O (adventitious carbon) and CF_2, respectively [60]. In addition, the peak near 532.5 eV of the O1s core electron spectrum for the pure PVDF (Figure 3(a.2)) is attributed to the combined effect of C=O (~531.2 eV), C-OH (~533 eV) and C-O (~534.1 eV) [60, 61]. Compared to the pure PVDF substrate, the variation of the peaks for the original and modified MOF based TFN membrane is mainly attributed to the nanoparticle additives. In addition, XPS spectra of Cr element for the original and IL-modified MIL-101 (Cr) are shown in Figure S15, where evident characteristic peaks of Cr $2p_{1/2}$ and Cr $2p_{3/2}$ are found for both materials. The combination of FTIR, XRF and XPS results confirms that the MIL-101 (Cr) based nanoparticle layer is successfully incorporated into the TFN membrane. Furthermore,

based on the XPS characterization shown in Figure 3, the elemental composition analysis on the original and IL-modified MOF-based TFN membrane is shown in Table S7.

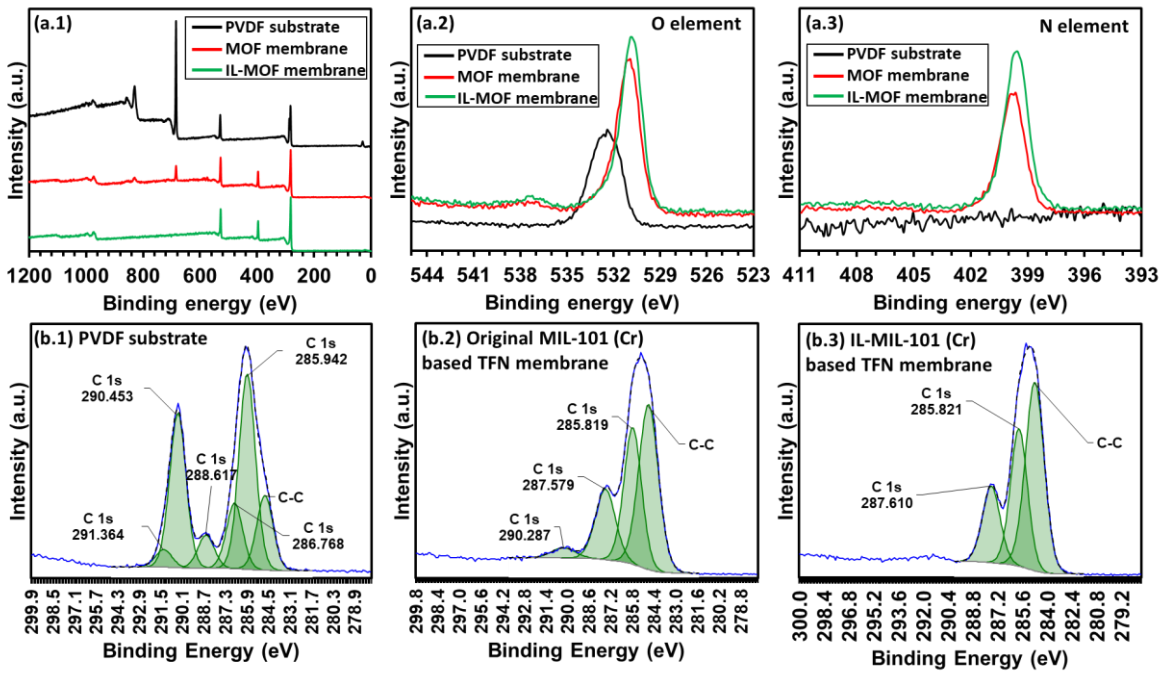

Figure 3: XPS (X-ray photoelectron spectroscopy) spectra of pure PVDF surface, original and modified MIL-101 (Cr) based TFN membrane surface.

Thickness and surface morphology

The cross-sectional SEM images of the membranes with different MOF loading amounts (M5, M10 and M15) are shown in Figure 4(a.1-a.3, respectively), from where the thickness of the selective layer and the substrate of the MIL-101 (Cr) based TFN membranes are observed. As shown in Figure 4(a.2), the thickness of the PVDF substrate is about 52.3 µm and the thickness of the selective layer for M10 is about 44.1 µm. When the amount of MOF encapsulation is halved (M5) or multiplied by 1.5 (M15), the thickness of the selective layer changes to ~31.0 µm (Figure 4(a.1)) and ~61.6 µm (Figure 4(a.3)), respectively. This suggests that the thickness of the MOF nanofiller layer increases as the MOF loading amount increases. It is noted that the presence of MOF at different loading levels may hinder or affect the IP efficiency between the PIP and TMC. In addition, the PVDF substrate remains almost the same as the MOF loading

increases. Figure 4(b.1-b.3) shows the wrinkled surface morphology of TFN membrane with different amount of ILs encapsulated MOF nanoparticles (it should be noted that the concentration of encapsulated ILs in the MOFs is the same for all three membranes M5, M10 and M15). In this work, the PVDF substrate is pre-soaked in aqueous solution containing PIP for some time and then removed. Organic solution containing TMC is then added to the top of the substrate to form the polyamide rejection layer. IL-MOF nanoparticles are introduced along with the aqueous solution. Step-growth polymerization occurs at the interface between these two immiscible phases, resulting in a polymer confined to the interface. It is noted that the wrinkled surface morphology of IP-related TFN membrane observed in this work has also been reported by other researchers [62, 63]. In addition, a uniform distribution of MIL-101 (Cr) MOF on the PVDF substrate is found for M5 (Figure 4(b.1)) and M10 (Figure 4(b.2)). However, aggregation of nanofillers is observed for M15 with increasing MOF encapsulation amount (Figure 4(b.3)). Furthermore, with higher MOF loading, MOFs layer is thick and hydrophilic which can reduce or hinder two solutions contact for IP reaction process. As discussed before, to ensure the homogeneity of the MOF-based TFN membrane, the original MOF is first encapsulated with the hydrophilic ionic liquids, which enhances the water affinity of MOF. Next, to improve the uniform distribution of IL-MOFs in water, the IL-MOFs based aqueous suspension is prepared by sonication instead of general stirring or shaking before IP reaction. In addition, during the vacuum filtration, the vacuum suction is operated under a moderate and controllable pressure, and the colloidal suspension is subsequently filtered. All these procedures ensure the homogeneity of the TFN membrane. Furthermore, the homogeneity of the TFN membrane is also supported by the surface outlook of the as-prepared membrane (as shown in Graphical Abstract) as well as the surface morphologies of the TFN membranes (as shown in Figure 4(b.2)). Furthermore, the elemental composition analysis on the original and IL-modified MOF is performed via EDS/elemental mapping technique, and the results are

given in Table S8. For reference, TGA curves for pure PVDF substrate, MOF loaded PVDF membrane (without IP reaction) and MOF based TFN membrane (with IP reaction) are shown in Figure S9, where promising thermal stability up to 400 °C are found for all the membranes.

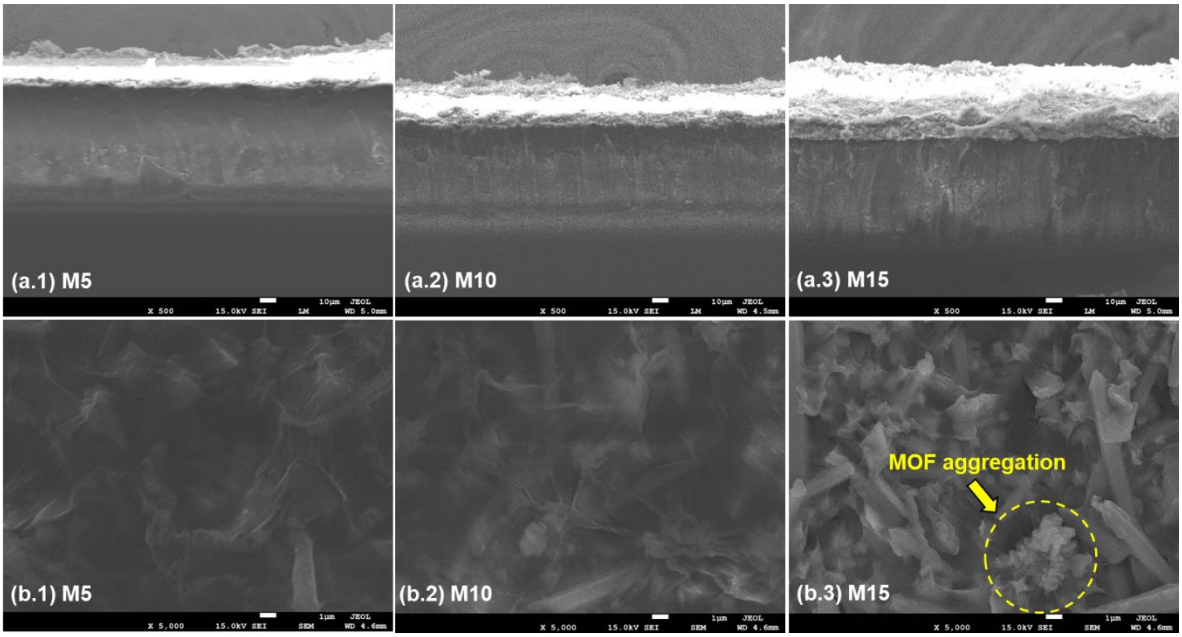

Figure 4: (a) Cross-sectional SEM pictures and (b) surface morphologies of MIL-101 (Cr) encapsulated PVDF based TFN membranes, with different MOF loading amounts (M5, M10 and M15, respectively 1, 2 and 3).

Surface roughness

The AFM 3D representation of original MOF based TFN membranes is shown in Figure 5, and the overall surface roughness analysis of all membranes are shown in Figure S10 and Table S3, where the surface roughness is evaluated by root mean square roughness (Rms), average roughness (Ra) and maximum vertical distance (Rz). Table 1 shows that the surface roughness of the membrane increases as the amount of MOF encapsulation increases. The lower roughness value of membrane represents a smoother dispersion of MOF nanofillers on the PVDF substrate. As the amount of MOF encapsulation increases, an obvious aggregation of MOF particles is observed, and the average surface roughness (M15) increases to 0.572 µm

(Figure S10 and Table S3). This increased roughness indicates a larger surface area of the MOF-TFN membrane, which has favorable effects on water permeation [64]. However, this makes it easier for the foulant to adhere to the membrane surface compared to surfaces with lower roughness, thus degrading the antifouling performance of the TFN membrane [65, 66].

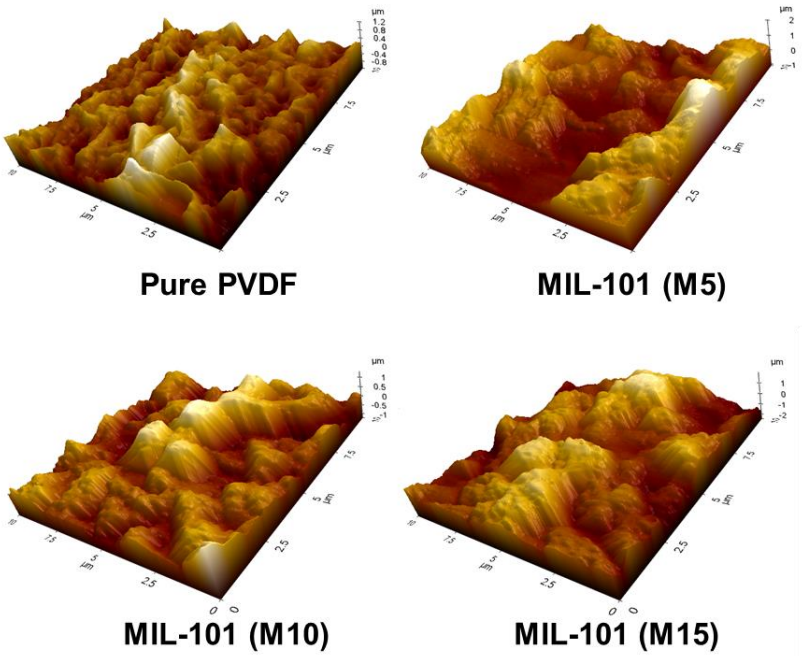

Figure 5: AFM images of pure PVDF substrate and MIL-101 (Cr) based TFN membranes, with different MOF loading amounts (M5, M10 and M15).

Table 1. The surface roughness parameters of pure PVDF substrate and MIL-101 (Cr) based TFN membranes, with different MOF loading amounts (M5, M10 and M15).

MOF type/amount	Rms (µm)	Ra (µm)	Rz (µm)
Pure PVDF membrane	0.313	0.240	2.332
MIL-101 (Cr) (M5)	0.434	0.345	2.524
MIL-101 (Cr) (M10)	0.622	0.519	3.136
MIL-101 (Cr) (M15)	0.705	0.572	4.410

Wettability

To test the effect of MOF loading on membrane performance, solution A, as discussed in the Methods section, is used with different volumes (5 ml/10 ml/15 ml) to fabricate the original MOF-based TFN membranes, designated M5, M10 and M15, respectively. Theoretically, the smaller the contact angle, the greater the hydrophilicity (wettability) of the fabricated membrane [67, 68]. From Figure 6(a.1-a.4), it can be observed that as the MOF loading increases, the water contact angle of the membrane decreases and hence the surface wettability increases. Figure 6(b) shows the average water contact angle analysis of TFN membranes, with the pure PVDF substrate tested for comparison. It is reported that the increased hydrophilicity would improve the antifouling performance and water permeability of the membrane [69]. The overall water contact angles of all membranes are shown in the supporting documents (Figure S11 and Table S4). Figure 6(b) also shows that the hydrophilicity of the original MIL-101 (Cr)-based TFN membrane could be further improved by ionic liquid encapsulation. The improved hydrophilicity of the ILs-MOF based TFN membrane is mainly attributed to the strong water adsorption ability of MIL-101 (Cr) MOFs and the affinity of the ionic liquid to water.

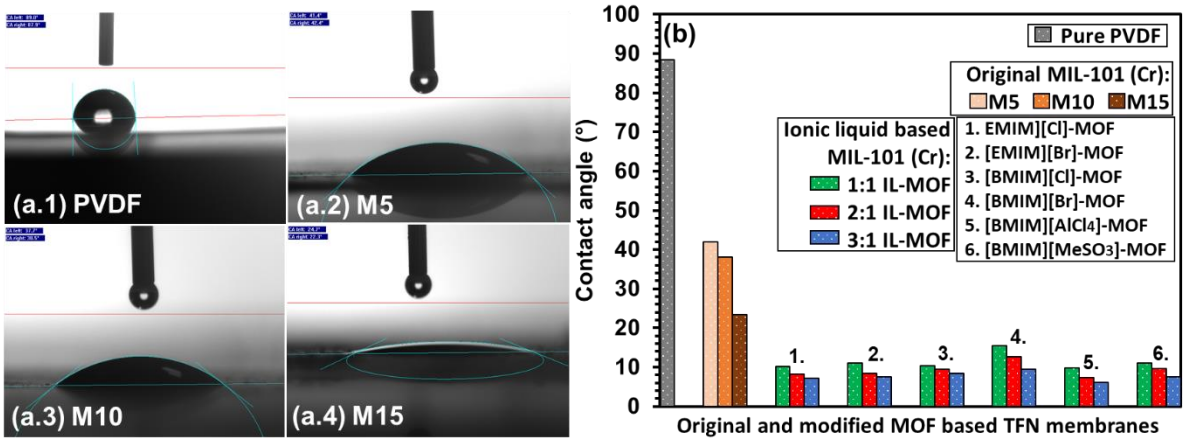

Figure 6: (a) Water contact angle screenshot for pure PVDF substrate and MOF based TFN membranes (with different MOF loading amounts (M5, M10 and M15)) and (b) the average contact angle analysis of original and modified membranes.

3.3 Lithium recovery performance

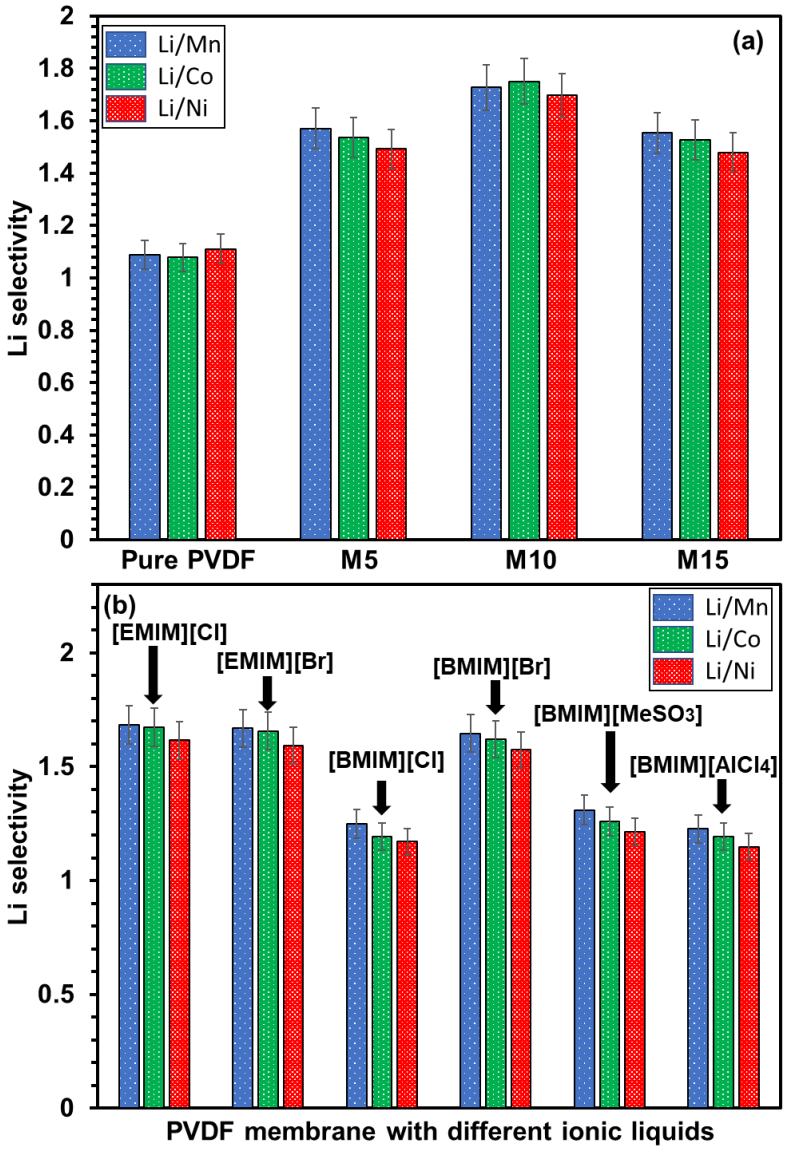

Figure 7: (a) Effect of MOF loading amount and (b) effect of ionic liquid encapsulated PVDF membrane on lithium selectivity.

Blank test

Figure 7(a) shows the effect of MOF loading on the lithium selectivity over Mn^{2+}, Co^{2+} and Ni^{2+}. The pure PVDF substrate is also tested for comparison purpose. It can be observed that pure PVDF does not show any obvious separation effect as the Li^{+} selectivity over Mn^{2+}, Co^{2+} and Ni^{2+} is less than 1.1. By loading original MIL-101 (Cr) to the PVDF surface (e.g. M5), $S_{Li^+, Mn^{2+}}$, $S_{Li^+, Co^{2+}}$ and $S_{Li^+, Ni^{2+}}$ are increased to 1.57, 1.72 and 1.55, respectively. The improved lithium selectivity is mainly due to the improved surface sinuosity of the MOF as

well as the polymer additives. The lithium selectivity $S_{Li^+,Mn^{2+}}$, $S_{Li^+,Co^{2+}}$ and $S_{Li^+,Ni^{2+}}$ could be further improved to 1.73, 1.75 and 1.69 respectively as more MOF is loaded (e.g. M10). This is because the surface voids for M10 are filled with more MOF nanoparticles. This makes it more difficult for the larger divalent metal ions to penetrate. However, as the amount of MOF loading continues to increase (e.g. M15), the lithium selectivity $S_{Li^+,Mn^{2+}}$, $S_{Li^+,Co^{2+}}$ and $S_{Li^+,Ni^{2+}}$ start to decrease to 1.49, 169 and 1.48, respectively. This is due to the fact that at excessive MOF loading, the nanoparticles tend to align or aggregate inappropriately (also confirmed by the SEM surface morphology study). Such clusters may act as defect sites on the TFN membrane surface and cause poor selectivity. Therefore, M10 membrane shows the best lithium recovery performance with the optimal MOF loading amount. It is noted that solution A containing original and modified MIL-101 (Cr) nanoparticles with a volume of 10 ml is used for the rest of the membrane study. In addition, no significant improvement in terms of lithium selectivity is obtained for the original MIL-101 (Cr) based TFN membrane compared to the pure PVDF membrane. This is mainly due to the fact that MIL-101 (Cr) has an extremely large pore size, which degrades the lithium separation process from other divalent metal ions.

Furthermore, six types of ionic liquids are separately encapsulated on the PVDF membrane (without MOF) via IP reaction and tested for lithium recovery experiment. As shown in Figure 7(b), all six types of ionic liquid encapsulated PVDF membranes show higher lithium selectivity compared to pure PVDF. The best performance is observed for [EMIM][Cl]-PVDF membrane, where the lithium selectivity $S_{Li^+,Mn^{2+}}$, $S_{Li^+,Co^{2+}}$ and $S_{Li^+,Ni^{2+}}$ are 1.68, 1.67 and 1.61, respectively. However, as with the original MOF-based TFN membrane, not much improvement is obtained in terms of lithium selectivity. Such a problem is mainly caused by the intrinsic shortcomings of the ionic liquid, such as relatively low stability and poor affinity to the polymeric component. In addition, the separation performance of PIP-TMC membranes are shown in Figure S13 in the supporting documents, where almost no

specific lithium separation are observed versus Mn^{2+} ($S_{Li^+, Mn^{2+}} = 1.035$), Co^{2+} ($S_{Li^+, Co^{2+}} = 1.036$) or Ni^{2+} ($S_{Li^+, Ni^{2+}} = 1.028$). Overall, membranes prepared by encapsulating only ionic liquid on the PVDF substrate without nanoparticle carriers are unstable and show poor selectivity.

Effect of ionic liquid

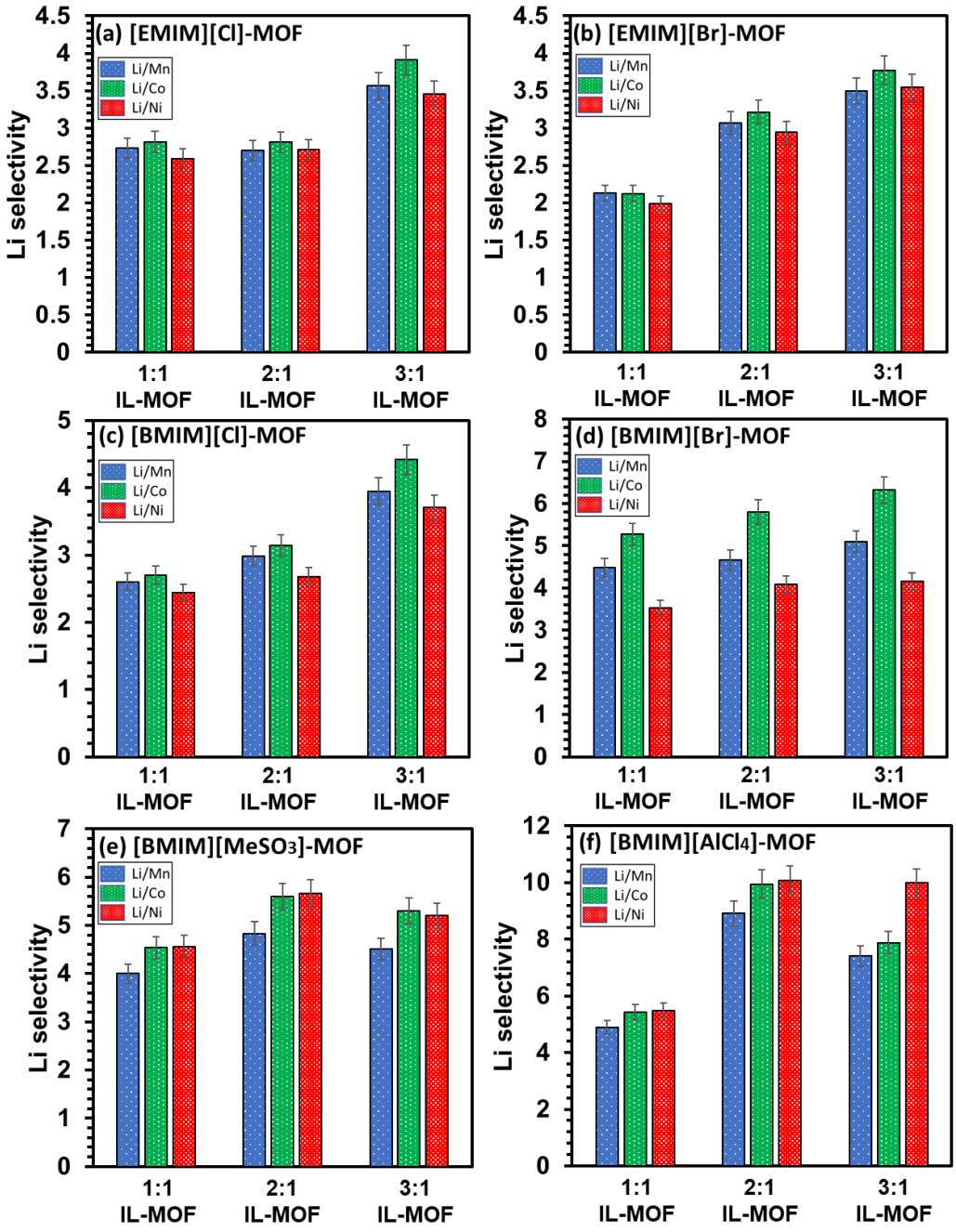

Figure 8: Lithium recovery experiments using various modified MOF based TFN membranes with different ionic liquid encapsulation amount.

Figure 8(a-f) shows the lithium recovery performances of different ionic liquid modified MIL-101 (Cr) based TFN membranes, from which one can observe the effect of the type and encapsulation amount (1:1 to 3:1) of the ionic liquid on the MOF framework. For example, Figure 8(a) shows that the lithium selectivity $S_{Li^+, Mn^{2+}}$, $S_{Li^+, Co^{2+}}$ and $S_{Li^+, Ni^{2+}}$ is 2.73, 2.81 and 2.59 respectively for 1:1 [EMIM][Cl]-MIL-101 (Cr) based TFN membrane. Similar results are found for 2:1 sample, and when the ionic liquid encapsulation is increased to 3:1, a significant improvement in terms of lithium selectivity $S_{Li^+, Mn^{2+}}$ (3.57, +30.7%), $S_{Li^+, Co^{2+}}$ (3.91, +39.1%) and $S_{Li^+, Ni^{2+}}$ (3.45, +33.2%) are obtained. This is because the ionic liquid encapsulation work enhances both the size exclusion effect (by reducing the pore opening of the original MOF) and the electrostatic repulsion (by modifying the membrane surface charge property). The combined effects result in higher lithium selectivity. In addition, [EMIM][Cl] has the smallest molecular size of all six types of ionic liquids. Therefore, a higher encapsulation ratio (3:1) is required for the TFN membrane to achieve optimal performance. Similar results are found for [EMIM][Br] (Figure 3(b), [BMIM][Cl] (Figure 3(c)) and [BMIM][Br] (Figure 3(d)), where the best performance is obtained at the highest ionic liquid encapsulation ratio (3:1). Furthermore, it is found that as the molecular size of the ionic liquid increases (from [EMIM][Cl] to [BMIM][Br]), the lithium selectivity $S_{Li^+, Mn^{2+}}$, $S_{Li^+, Co^{2+}}$ and $S_{Li^+, Ni^{2+}}$ increase up to 5.10, 6.32 and 4.16 for 3:1 [BMIM][Br]-MIL-101 (Cr) based TFN membrane. These results prove that larger ionic liquid with higher encapsulation amount will further enhance the sieving effect and electrostatic repulsion effect, leading to higher lithium selectivity. However, for ionic liquid with even larger molecular size such as [BMIM][$MeSO_3$] (Figure 8(e)) and [BMIM][$AlCl_4$] (Figure 8(f)), the overall optimal lithium recovery performance is obtained at the median encapsulation ratio (2:1). This is mainly due to the fact that the large ionic liquid encapsulation ratio of 2:1 has already reached the MOF encapsulation limit. After that, any more ionic liquid will not be successfully encapsulated into the MOF

framework and it may also degrade the ionic liquid-MOF interaction. The overloaded ionic liquid will also occupy excess pore space, preventing lithium ions from permeating through the membrane surface. Therefore, decreased lithium selectivity is found for both the 3:1 [BMIM][$MeSO_3$]-MOF and [BMIM][$AlCl_4$]-MOF based TFN membranes. Furthermore, among all the membranes, the 2:1 [BMIM][$AlCl_4$] modified MOF based TFN membrane exhibits the highest lithium selectivity $S_{Li^+, Mn^{2+}}$ (8.91), $S_{Li^+, Co^{2+}}$ (9.94) and $S_{Li^+, Ni^{2+}}$ (10.08). Taken together, these results suggest that the lithium recovery performance of the modified MOF-based TFN membrane is closely related to the type and amount of encapsulated ionic liquid, which is internally controlled by the ionic liquid property (such as size and compatibility) as well as the ionic liquid-MOF interaction.

Separation mechanism

Figure 9(a) shows the best lithium recovery performance for each membrane type used in this work. The overall performance in terms of lithium selectivity could be ranked as IL-MOF based TFN membrane > MOF based TFN membrane > pure PVDF substrate. From the original MOF based TFN membrane to the modified MOF based TFN membrane, +415%, +468% and +497% improvement in terms of lithium selectivity $S_{Li^+, Mn^{2+}}$ (from 1.73 to 8.91), $S_{Li^+, Co^{2+}}$ (from 1.75 to 9.94) and $S_{Li^+, Ni^{2+}}$ (from 1.69 to 10.09) are obtained, respectively. The separation mechanisms of TFN membranes mainly include sieving effect (size exclusion effect) and electrostatic interaction. Compared with the parent MIL-101 (Cr) based TFN membrane, the ILs encapsulated MIL-101 (Cr) (IL-MIL-101 (Cr)) based TFN membrane has the following advantages: (i) smaller free apertures. The ILs additives occupy a fraction of the free space of the opening pores of the original MIL-101 (Cr). Therefore, the encapsulation of the ILs guests with long chains in the abundant voids tailors the pore size distribution of the parent MIL-101 (Cr), resulting in reduced pore sizes or free apertures; and (ii) enhanced electrostatic repulsion

due to more positively charged membrane surface. Table S2 and Figure 9(b.1) show the micropore and total pore volumes of the original and modified MIL-101 (Cr) based MOFs. The total pore volume of the original MIL-101 (Cr) is 1.197 cm^3/g. By encapsulating IL into the MOF, the total pore volume is reduced to between 1.04 and 1.15 cm^3/g (depending on the type and amount of IL encapsulated). In addition, the micropore volume of the IL modified MOF increases significantly from 0.14 cm^3/g to approximately 0.30 cm^3/g compared to the original MIL-101 (Cr). Therefore, the microporosity ($= \frac{\text{micropore volume}}{\text{total pore volume}}$) of the original and modified MIL-101 (Cr) based MOFs are shown in Figure 9(b.2). It can be observed that the micro-porosity of MIL-101 (Cr) is enriched by IL encapsulation. In fact, the micro-porosity increased from 0.117 to about 0.295 cm^3/g, indicating that larger pores of MIL-101 (Cr) were converted into micro-pores by IL encapsulation, which improves the size exclusion (sieving) effect of the MOF particles during metal ion separation.

Based on the solubility-diffusivity theory, there are two continuous steps in pressure-driven ion transfer across TFN membranes: (i) adsorption and dissolution of ions at the membrane surface and (ii) diffusion through the membrane channels [70]. The electrostatic repulsion between the ions and the membrane plays a crucial role in the selective separation of metal ions. The surface charge of the TFN membrane affects the retention and transport of metal ions. Based on zeta potential analysis (Figure 9(c.1)), the TFN membrane surface is positively charged under acidic condition ($2 \leq pH \leq 6$). Theoretically, due to the electrostatic repulsion force, a more positively charged membrane surface tends to provide a stronger rejection effect for positive ions, especially divalent ions such as $Ni^{2+}/Co^{2+}/Mn^{2+}$. In fact, many works have pointed out that positively charged membranes with enhanced electrostatic repulsion are suitable for removal of multivalent cations from wastewater [2, 71]. MOFs with cationic functional groups and positively charged metal centers are usually adopted for the preparation of positively charged membranes. ILs often contain such cationic functional groups (such as hydroxy and amine

groups) and have a strong affinity to MOFs. This results in more positively charged membrane surface (Figure 9(c.1-c.2)) and enhanced electrostatic repulsion for IL-MOF based TFN membrane. Together, these factors contribute to the improved lithium selectivity of IL-MIL-101 (Cr) incorporated TFN membranes.

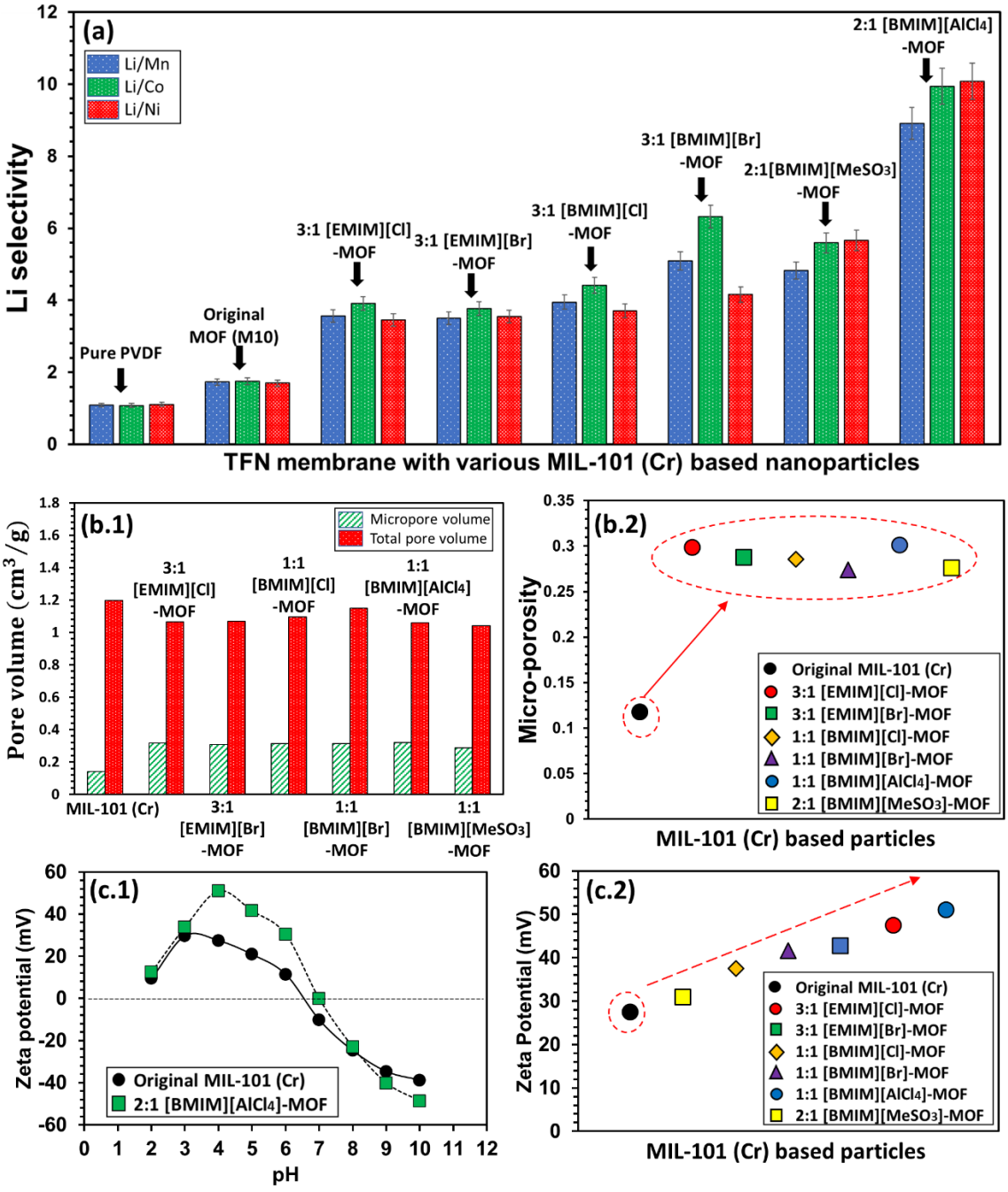

Figure 9: (a) the highest lithium selectivity of pure PVDF substrate, original and modified MOF based TFN membranes; (b.1) pore volume analysis of original and modified MIL-101 (Cr),

(b.2) micro-porosity analysis of original and modified MIL-101 (Cr) particles; (c.1) Zeta potential analysis of original MOF and 2:1 [BMIM][$AlCl_4$]-MIL-101 (Cr) for pH ranges from 2 to 10, (c.2) Zeta potential analysis of all the original and modified MIL-101 (Cr) at pH = 4.

Effect of other relevant factors

Overall, the lithium recovery efficiency of the nanofiltration (NF) system is controlled by three factors: (i) membrane properties (such as surface roughness, wettability and antifouling behavior); (ii) metal ion properties (such as diffusivity and size); and (iii) operating conditions (such as filtration pressure, temperature and time). In addition to the revised membrane properties discussed above, the difference in rejection efficiency between Li^+ and other divalent metal ions (such as Ni^{2+}, Co^{2+} and Mn^{2+}) is also attributed to the properties of these ions. Properties related to metal ion separation in aqueous environments, such as hydration radius and diffusivity, are presented in Table S5 for a comprehensive understanding. It can be observed that Li^+ has the smallest hydrated radius and Stokes radius compared to the divalent metal ions. Due to the sieving mechanism (or size exclusion effect) of the TFN membrane, smaller Li^+ easily permeate through the membrane while the majority of larger divalent metal ions are blocked. In addition, the highest diffusivity of Li^+ result in the lowest retention by the TFN membrane. Furthermore, it has been reported by Zheng et al. [72] that the precipitation of the metal hydroxides would also affect the lithium recovery efficiency. In that work, they report that based on the solution-diffusion model, the solute firstly sorbs on the membrane surface on the feed side and diffuses through the membrane matrix. Finally, the solute desorbs at the permeate side of the membrane. Thus, the separation efficiency is governed by the solubility and diffusivity of the solutes. It should be noted that the anions of the heavy metal salts used in that work are chloride and nitrate (in our work it is chloride). Compared with divalent heavy metal cations, H_3O^+ has a smaller charge and a smaller size, making it is easier to pass through the membrane to achieve the charge balance with Cl^- or NO_3^- in the permeate

solutions. As the majority of the larger divalent metal ions are retained on the feed side, H^+ (also of smaller size) preferentially diffuse across the membrane to balance the anions in the permeate solution. Therefore, both divalent metal ions and OH^- ions concentrations increase at the porous surface. Consequently, precipitation of divalent metal hydroxide occurs when K_{sp} (solubility product constant) is reached and rejection of metal ions occurs. In addition, other factors such as pH and concentration of the feed solution, transmembrane pressure, and operating time also affect the lithium recovery efficiency. For example, Wu et al. [73] reported that a low pH (< 7) was favorable for lithium ions to pass through the membrane because the Li^+ recognition sites on the membrane surface were protonated at low pH and prevent Li^+ from binding to the membrane. In another study, Bi et al. [74] reported that low pH (< 7) was preferable for the separation of Li^+ and Mg^{2+}, due to the elevated dielectric exclusion to multivalent ions. The pH of our LIB leaching solution is 3.51, making it suitable for the recovery of lithium from other divalent metal ions. On the other hand, Kumar et al. [75] reported that increasing the transmembrane pressure from 5 to 10 bar resulted in about a 6% increase in rejection efficiency for divalent metal ions (such as Ni^{2+}, Co^{2+} and Mn^{2+}) and a marginal retention effect for monovalent metal ions (Li^+). This study showed an increased separation efficiency of Li^+ over these divalent metal ions. A reasonable explanation for this phenomenon is that the uncoupling of the solvent and solute fluxes, as well as the solution-diffusion mechanism, caused the solvent flux to increase at higher pressures and the solute flux to remain almost the same. Thus, for a constant feed solution concentration, the rejection rate of the solution was increased (especially for divalent metal ions with larger size and lower diffusivity). In addition, it is known that membrane fouling would reduce the rejection efficiency for all metal ions over long periods of operation. However, this problem could be overcome by applying membrane regeneration. In this study, the transmembrane pressure is

maintained at 5 bar to achieve both the promising lithium recovery and relatively fast water flux at low pressure.

3.4 Water permeance, regeneration, antifouling performance

Figure 10(a) and Figure 10(b) show the water flux and permeability of the TFN membrane, respectively. Here, the modified MOF (i.e. 2:1 [BMIM][$AlCl_4$]-MOF) based TFN membrane with the highest lithium selectivity is selected for comparison. For the original MOF-based TFN membrane, Figure 10(a) shows that the water flux is approximately linear proportional to the transmembrane pressure. As the pressure increases from 2.5 bar to 15 bar, the water flux of the original MOF based TFN membrane increases from 88.1 LMH to 393.4 LMH. In addition, Figure 10(b) shows a promising low pressure permeability (35.3 L/(m^2·h·bar) at 2.5 bar). It also shows a relatively stable permeability at higher pressures (around 25.0 L/(m^2·h·bar) at pressures above 5 bar). The promising permeability is mainly attributed to the hydrophilic MIL-101(Cr) synergy on the polyamide selective layer: (i) the presence of voids at the interface between the polymer and the nanocomposite additives promotes the diffusion and solubilization of water molecules through the membrane; (ii) water molecules are transported via shorter flow paths of the internal channels of the MOFs, which accelerates the diffusion of water; and (iii) the contact area between the feed solution and the membrane is increased as a result of the "ridge and valley" surface morphology of the TFN membrane. Furthermore, both higher water flux and higher permeability are found for the modified MOF-based TFN membrane. For example, at low pressure (2.5 bar), the water flux and permeability are 112.4 LMH and 45.0 L/(m^2·h·bar) respectively, which is 27.6% higher than that of the original MOF-based TFN membrane. These results prove that the reported membrane is suitable for low pressure driven metal ion separation applications. Compared with the original MOF-based TFN membrane, the IL-MOF-based TFN membrane has higher ionic conductivity and improved hydrophilicity. The improved ionic conductivity of IL-MIL-101(Cr) is due to the increased

pore-filling fraction [76] of MIL-101 (Cr) as well as the synergistic effect of MOFs and ILs [77]. Subsequently, the IL guests form an ion transport network and promote conduction in the pore channels. Therefore, the ion transfer pathways through the IL-MIL-101 (Cr) based TFN membranes are significantly tuned and higher permeability is achieved.

The regeneration performance of the original and modified TFN membranes is shown in Figure 10(c). It is found that for the original membrane, the permeability gradually decreases with the feed solution flow up to 1 L. After that, regeneration work is performed and the permeability is restored to the original level. A similar behavior is found for the modified membrane with less permeability degradation. In addition, negligible degradation of the surface morphology of the TFN membrane was observed before lithium recovery experiment (Figure 10(c.1)), after lithium recovery experiment (Figure 10(c.2)) and after regeneration (Figure 10(c.3)), which further proved the stability of the as-prepared TFN membrane. Furthermore, Figure 10(d) shows the antifouling performance for both the original and modified MOF-based TFN membranes. The FRR decreases monotonically with increasing transmembrane pressure. In addition, a better antifouling performance is obtained for the modified MOF-based TFN membrane (86.8% < FRR < 96.4%) compared to the original one (76.4% < FRR < 88.2%). Membrane fouling is mainly attributed to the accumulation of heavy metal ions on the surface of the TFN membrane. It is well known that the fouling susceptibility of TFN membrane is related to the interplay of surface electrostatic repulsion, steric hindrance, surface tension and wettability.[78] The improved fouling resistance and reversibility of the TFN membrane is mainly attributed to two facts: (i) the selective coating of the polyamide with hydrophilic IL-MOF nanoparticle additives creates a hydrated thin film. The hydrated thin film prevents the foulant from adsorbing on the membrane as the water movement consumes the free energy of the system;[79] and (ii) the enhanced electrostatic interaction between the charged membrane

surface and the BSA foulant prevent the BSA from depositing on the membrane. Both factors result in improved fouling control and extended TFN membrane life.

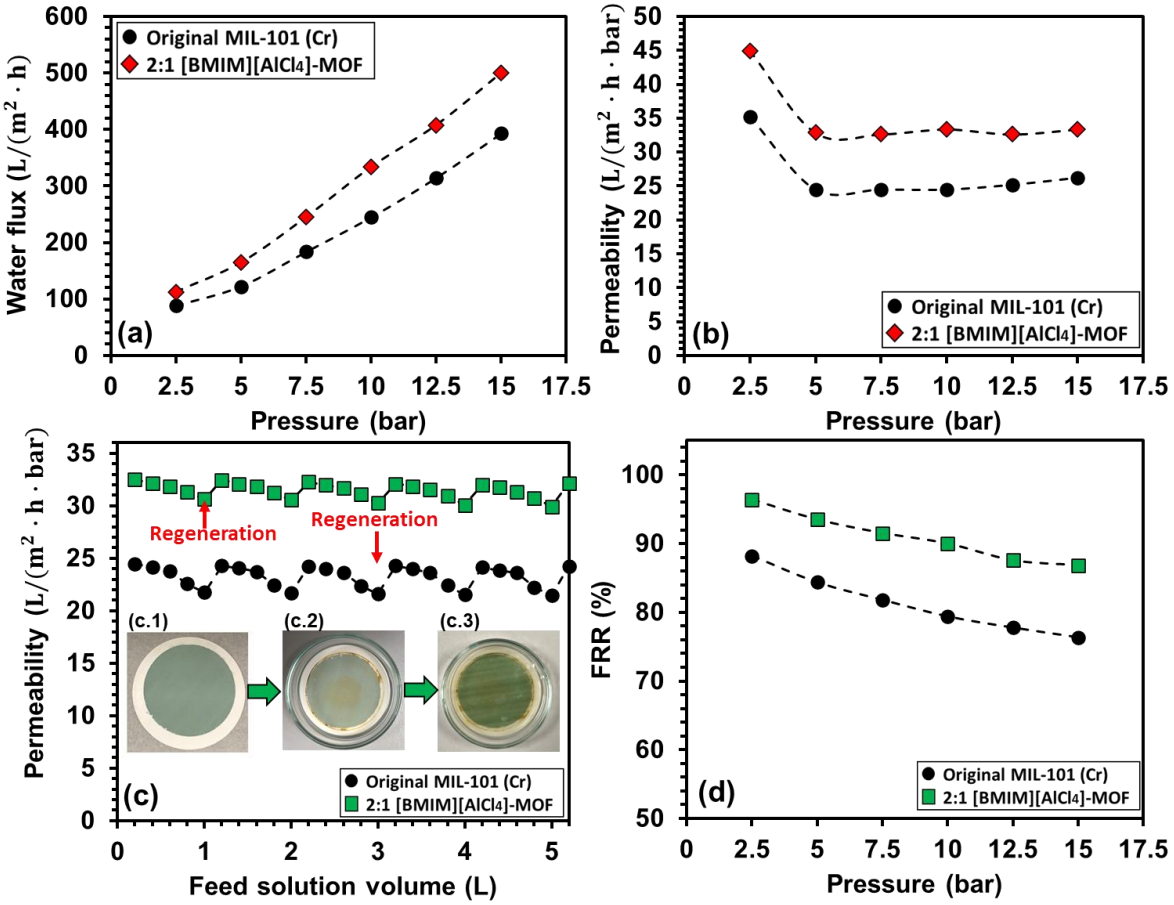

Figure 10: Performance assessment of original and modified MIL-101 (Cr) based TFN membrane in terms of (a) water flux; (b) permeability; (c) regeneration and (d) antifouling performance.

3.5 Antiaging performance

The investigation on the leaching tendency of ILs from MOFs was performed on 2:1 [BMIM][$AlCl_4$]-MOF TFN membrane after multiple separation cycles by ATR-FTIR analysis, and have been compared to the fresh IL-MOF TFN membrane. As shown in Figure 11(a), the peak at 1617 cm^{-1} is more intense because of C=C and N=C=N stretching of the imidazolium cation ring of the IL. C=C and C=N stretching of the imidazolium ring are also responsible of the bands at 1545 and 1509 cm^{-1}. Symmetric and asymmetric stretching of CH_2 and CH_3 in the

IL cause the intensification of the bands at 1470 cm^{-1} and 1440 cm^{-1}. The peak at 1166 cm^{-1} also covers the CH_3-N stretching of $[BMIM]^+$ in addition to the CF2 stretching of PVDF. C-N stretching vibration is present in the band at 829 cm^{-1}. The peak at 747 cm^{-1} and the one appearing at 659 cm^{-1} are related to plane and out-of-plane imidazolium bending, respectively. For each ATR-FTIR bands, the more the membrane was used, the more the intensity of the band decreases (transmittance increases). This may indicate that the IL-MOF layer is slightly washed and becomes thinner after separation test. Areas of characteristic ATR-FTIR bands have been calculated and compared between each membrane before and after filtrations, as illustrated in Figure 11(b). The calculated areas are also given in the supporting documents Table S6. Averaged over all peaks, after the 1st filtration the membrane lost 1.6% for each FTIR band, 5.8% more between the 1st and the second filtration, 5.9% after the 3rd one and 1.5% between the 3rd and the 4th filtration. One can also note that the decrease of ATR-FTIR intensity and area are not constant from one separation test to another.

Detachment of nanoparticles not only results in surface defects of membrane, but also causes pollution to the permeate solution. Figure 11(c) shows the indirect evaluation on the detachment tendency of MOF nanoparticles from TFN membrane by tracking the chromium concentration. It is therefore observed that as time passes, the concentration of chromium ions increases linearly (R linear regression with $R^2 = 0.9637$) from 0.118 mg/L to 0.179 mg/L (less than 0.2 mg/L) from the first hour to the twelfth hour, respectively. It can then be calculated that the detachment percentage of MOF is as low as 0.54% over 12 hours, which proves the promising adhesion between MOF nanoparticles, PA matrix and the substrate. In addition, to test the lithium recovery effect of the TFN membrane, multi-filtration experiments were carried out. Typically, the simulated LIBs leaching solution was used as the feed solution for the first filtration cycle. After that, the permeate solution was collected and used as the feed solution for the second filtration cycle. The permeate solution in the second filtration cycle was then

used as the feed solution for the third filtration cycle. Same procedure was applied until the fifth filtration cycle. The lithium ions concentration of the permeate solution after each filtration cycle was tested by ICP and shown in Figure 11(d). By repeatedly filtrating the solution, the lithium ions were concentrated. It is found that the lithium concentration in permeate solution increases almost linearly (from 393.3 mg/L to 744.5 mg/L) for the first three filtration cycles. The concentration of lithium ions after the fourth and fifth cycle is 802.7 mg/L (93.9% recovery rate with respect to the feed solution) and 846.2 mg/L (98.9% recovery rate with respect to the feed solution), respectively. All these results discussed above prove that the IL-MOF-based TFN membrane could recover lithium ions from LIBs leachate with promising membrane integrity.

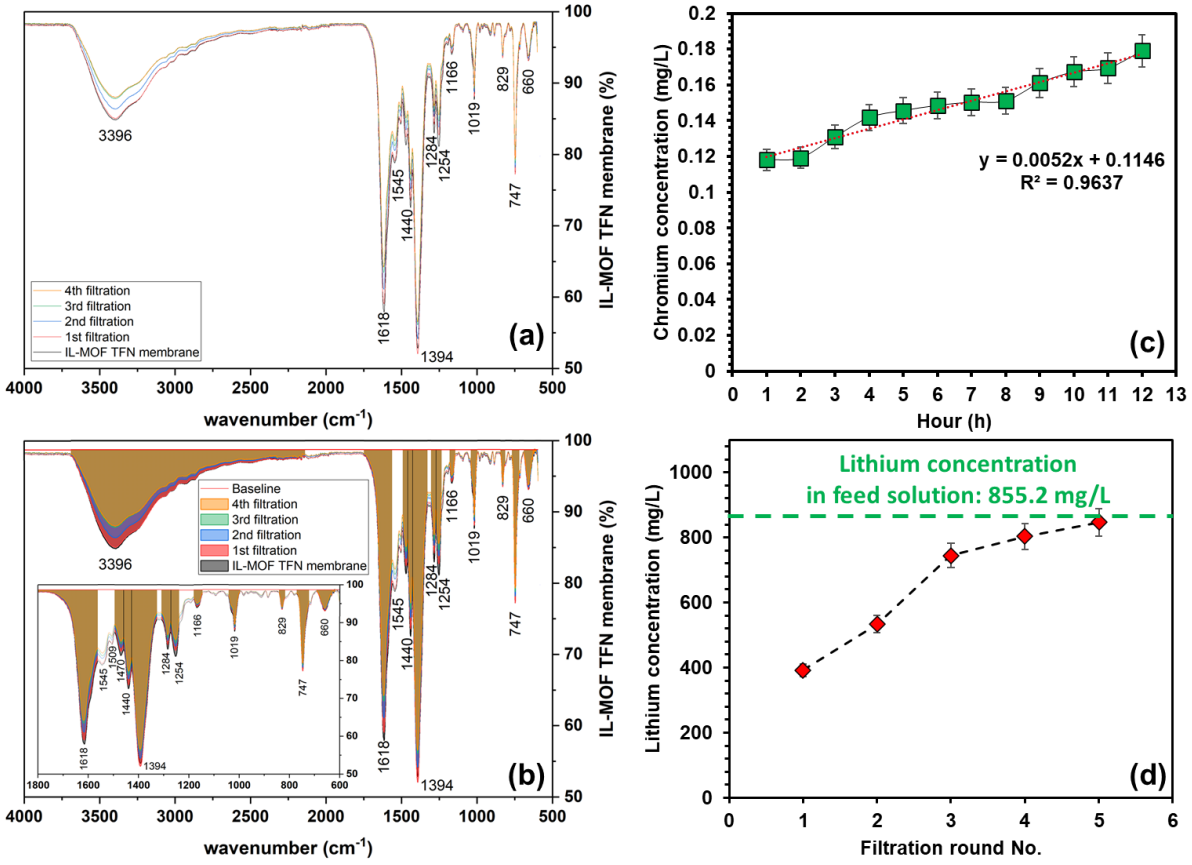

Figure 11: (a) ATR-FTIR profiles for 2:1 [BMIM][$AlCl_4$]-MIL-101 based TFN membrane before and after filtration; (b) ATR-FTIR profiles for 2:1 [BMIM][$AlCl_4$]-MIL-101 based TFN membrane before and after filtration, showing the area for each membrane; (c) evaluation of detachment tendency of MOF-based nanoparticles from M15 TFN membrane; and (d) the lithium concentration of permeate solution after each separation cycle.

3.6 Comparison study

The state-of-the-art membrane-based technologies for lithium recovery from water resources are classified into seven categories, namely permselective exchange membrane capacitive deionization (PSMCDI) [80], selective electrodialysis (S-ED) [81], membrane distillation crystallization (MDC) [82], ion sieve membrane (ISM) [83], ion imprinted membrane (IIM) [84], supported liquid membrane (SLM) [10] and nanofiltration (NF) membrane [85]. Compared to other membrane technologies, NF is the only commercially available large-scale lithium recovery process due to its high technological maturity, high cost efficiency and low operational complexity [2]. Criteria such as lithium selectivity, permeability, stability, antifouling, antiaging and regeneration performance are important for TFN membranes used in the NF field for lithium recovery. These criteria are closely related to the TFN membrane properties such as wettability, surface roughness, surface charge, and nanoparticle detachment tendency. For example, higher surface roughness leads to higher surface area, which leads to higher water permeability [64]. Over the past decades, it has been known that higher surface roughness would degrade the antifouling performance of the TFN membrane because foulants would more easily adhere to the rougher surface. Recently, however, Gan et al. [86] proposed that a lower fouling tendency was observed in the rough membrane containing nanovoids, which was attributed to the weakened "funnel effect" as well as the reduced average localized flux over the membrane surface. In our work, the average surface roughness of IL-MOF-TFN membranes is comparable to that of MOF-TFN membranes (Figure S10 and Table S3). The

higher water permeability and better antifouling performance are mainly attributed to the IL additives. In addition, the fabrication of defect-free TFN membranes is crucial for the size-sieving-based resource recovery process in the aqueous environment. For example, Aljubran et al. reported a defect-free interfacially-polymerized TFC membrane with ultrahigh As (III) rejection (> 99.8%) [87]. The surface defects of the TFN membrane are closely related to the loading level of the nanoparticles. Neither too little (not enough to cover the membrane surface uniformly) nor too much (tends to form aggregates) of nanoparticle loading would cause surface defects. In this work, membranes with different loading amounts of IL-MOF nanofillers are characterized by various techniques (such as AFM and SEM), and membranes with the optimized IL-MOF loading are used for further investigation. Furthermore, the performance of the TFN membrane is directly related to the nanoparticle materials [88]. For example, Shao et al. [89] used the dispersant-poly (maleic acid-co-acrylic acid) sodium slat (PMAS) to promote the membrane formation. The PMAS was found to improve the particle deposition behaviour and interfacial compatibility. Research works have reported that ILs [90, 91] or MOFs [92] can be used alone in the field of membrane-based lithium recovery. In our study, by encapsulating ILs into the MOFs, the larger pore size of the original MOFs is reduced and the leaching tendency of the ILs is decreased. The synergistic effect between ILs and MOFs simultaneously strengthens the TFN membrane. In the recent literature, the water permeability of the majority of TFN membranes ranges from 25.0 L/(m^2·h·bar) to 55.0 L/(m^2·h·bar) (ours is 45.0 L/(m^2·h·bar)), which mainly depends on the types of feed solution, membrane configuration and operating conditions. Finally, it should be noted that our results (lithium selectivity around 10) may not be remarkable compared to other lithium selectivity reported in the literature. The key challenges of ILs encapsulation in the MOFs are (i) to precisely control on the amount of ILs encapsulation; and (ii) to prevent ILs leaching. First of all, ambiguous ILs encapsulation would degrade the performance of the TFN membrane. Insufficient ILs encapsulation results

in poor $S_{Li^+,Mn^{2+}}$, $S_{Li^+,Co^{2+}}$ and $S_{Li^+,Ni^{2+}}$, and excess ILs encapsulation leads to the unstable bonding between the IL additives and the MOF structure. Secondly, ILs leaching from the MOF structure would not only cause the decrease of the separation performance, but also pollute the permeate solution. Both challenges could be systematically overcome by precise encapsulation of the ILs into the MOFs, where dehydration and creation of coordinatively unsaturated chromium sites (CUS) of the original MOF are performed. Thus, the ILs are chemically bound to the secondary building unit (SBU) of the MOF. In addition to the challenges mentioned above, another major limitation of this technique is the relatively high cost of ILs for practical implementation and scalability, and this is one of the most common limitations of using ILs for various applications. However, this work provides a novel approach for the fabrication of TFN membranes with tunable size-selective effect. By verifying the type and encapsulation amount of ILs, the synthesized membrane could be used in various applications such as desalination, wastewater treatment, and resource recovery. At present, the use of IL-MOF-based membranes for lithium recovery is still in the early stages of research and laboratory benchmark, at technology readiness level of 3. More efforts should be made on membrane scale-up, economic analysis and industrial implementation aspects. These will likely involve intellectual property development and is beyond the scope of this article.

4. Conclusions

This paper demonstrates a tailorable and hierarchical approach to the fabrication of ionic liquid encapsulated MIL-101 (Cr) based thin film nanocomposite membranes for lithium recovery. The fabrication and characterization of the nanoparticles and membranes, as well as the lithium recovery experiments are reported. Compared to the original MOF-based TFN membrane, the main improvements of the ionic liquid encapsulated membranes are summarized as follows:

(i) the modified TFN membrane shows promising mechanical strength and flexibility with improved sieving effect and electrostatic repulsion to divalent ions;

(ii) the modified TFN membrane exhibits a fourfold improvement in lithium selectivity (up to 10) over Mn, Co and Ni;

(iii) improved regeneration behavior, permeability (up to 45.0 L/(m^2·h·bar)), antifouling performance (flux recovery rate FRR up to 96.39%), antiaging and stability behaviors are achieved.

Overall, with this report of high Li^+ metal ion separation efficiencies on simulated LIBs lixiviates, as well as membrane regeneration, antifouling and antiaging properties, we have already gone well beyond a simple proof of concept, thus demonstrating the potential of the proposed tailorable membrane fabrication method for various metal ion separation applications. In other words, the as-synthesized IL-MIL-101 (Cr)-based TFN membrane proves to be a promising candidate for efficient lithium recovery, but probably also for other lixiviates. Further investigation into product quality, operating costs, system stability, refining the ILs encapsulation amount, energy requirements and membrane optimization will be explored in future research.

Conflicts of interest

The authors declare no competing financial interest.

Acknowledgements

The authors acknowledge financial support from the SCARCE project, which (i) phase 1 was supported by the National Research Foundation, Prime Minister's Office, Singapore, the Ministry of National Development, Singapore, and National Environment Agency, Singapore under its Closing the Waste Loop R&D Initiative as part of the Urban Solutions & Sustainability – Integration Fund [Award No. USS-IF-2018-4] and; (ii) Phase 2 is currently supported by the National Research Foundation, Singapore, and National Environment Agency, Singapore under its Closing the Waste Loop Funding Initiative (Award CTRL-2023-1D-01). H.B. thanks Dr. Joseph Jeganroy for the supply of a typical composition of a LIBs (NMC)

leaching solution. H.B. thanks Mr. Eric Tan Rui Wen and Miss. Aishwarya D/O Ravindran for the acquisition of FTIR, TGA and wettability data.

Author contributions

The conceptualization was by H. B. and J. C. G. The methodology was by H. B. and S.C. The investigation was performed by H.B., and results were interpreted together with S.C. and J.C.G. Funding acquisition was by J.C.G. and Y.QY., and project administration by J.C.G. and S.C. Supervision was by J.C.G. and Y.QY. Writing first draft was done by H.B. All authors reviewed and edited the paper.

Appendix A. Supplementary Information (SI)

Nomenclature

AFM	Atomic force microcopy
ATR-FTIR	Attenuated total reflection-Fourier transform infrared
BAS	Bovine Serum Albumin
BET	Brunauer-Emmett-Teller
D	Density conversion factor
D_{MOF} *(%)*	Detachment percentage of MOF
EDX	X-ray energy dispersive spectroscopy
FRR	Flux recovery rate
FTIR	Fourier transmission infrared
LIB	Lithium-ion battery
MIL	Materials Institute Lavoisier
MOF	Metal-organic framework
NCM	Non-contact mode
NF	Nanofiltration
PA	Polyamide
PCP	Porous coordination polymer
PVDF	Polyvinylidene fluoride

FESEM	Filed emission scanning electron microscope
TFC	Thin film composite
TFN	Thin film nanocomposite
TGA	Thermalgravimetric Analysis
WCA	Water contact angle
XPS	X-ray photoelectron spectroscopy
XRD	X-ray diffraction
XRF	X-Ray Fluorescence

References

1. Harper, G., R. Sommerville, E. Kendrick, L. Driscoll, P. Slater, R. Stolkin, A. Walton, P. Christensen, O. Heidrich, and S. Lambert, *Recycling lithium-ion batteries from electric vehicles.* nature, 2019. **575**(7781): p. 75-86.
2. Li, X., Y. Mo, W. Qing, S. Shao, C.Y. Tang, and J. Li, *Membrane-based technologies for lithium recovery from water lithium resources: A review.* Journal of Membrane Science, 2019. **591**: p. 117317.
3. Choi, H.-B., J.-S. Ryu, W.-J. Shin, and N. Vigier, *The impact of anthropogenic inputs on lithium content in river and tap water.* Nature communications, 2019. **10**(1): p. 1-7.
4. Turcheniuk, K., D. Bondarev, V. Singhal, and G. Yushin, *Ten years left to redesign lithium-ion batteries*. 2018, Nature Publishing Group.
5. Li, W., C. Shi, A. Zhou, X. He, Y. Sun, and J. Zhang, *A positively charged composite nanofiltration membrane modified by EDTA for LiCl/MgCl2 separation.* Separation and Purification Technology, 2017. **186**: p. 233-242.
6. Ciez, R.E. and J. Whitacre, *Examining different recycling processes for lithium-ion batteries.* Nature Sustainability, 2019. **2**(2): p. 148-156.
7. Xu, X., Y. Chen, P. Wan, K. Gasem, K. Wang, T. He, H. Adidharma, and M. Fan, *Extraction of lithium with functionalized lithium ion-sieves.* Progress in Materials Science, 2016. **84**: p. 276-313.
8. Lei, S., W. Sun, and Y. Yang, *Solvent extraction for recycling of spent lithium-ion batteries.* Journal of Hazardous Materials, 2022. **424**: p. 127654.
9. Sun, D., M. Meng, Y. Qiao, Y. Zhao, Y. Yan, and C. Li, *Synthesis of ion imprinted nanocomposite membranes for selective adsorption of lithium.* Separation and Purification Technology, 2018. **194**: p. 64-72.
10. Zante, G., M. Boltoeva, A. Masmoudi, R. Barillon, and D. Trebouet, *Highly selective transport of lithium across a supported liquid membrane.* Journal of Fluorine Chemistry, 2020. **236**: p. 109593.
11. Song, Y. and Z. Zhao, *Recovery of lithium from spent lithium-ion batteries using precipitation and electrodialysis techniques.* Separation and Purification Technology, 2018. **206**: p. 335-342.
12. Quist-Jensen, C.A., A. Ali, S. Mondal, F. Macedonio, and E. Drioli, *A study of membrane distillation and crystallization for lithium recovery from high-concentrated aqueous solutions.* Journal of Membrane Science, 2016. **505**: p. 167-173.
13. Nativ, P., O. Lahav, and Y. Gendel, *Separation of divalent and monovalent ions using flow-electrode capacitive deionization with nanofiltration membranes.* Desalination, 2018. **425**: p. 123-129.

14. Zhu, J., J. Hou, S. Yuan, Y. Zhao, Y. Li, R. Zhang, M. Tian, J. Li, J. Wang, and B. Van der Bruggen, *MOF-positioned polyamide membranes with a fishnet-like structure for elevated nanofiltration performance.* Journal of Materials Chemistry A, 2019. **7**(27): p. 16313-16322.
15. Feng, X., D. Peng, J. Zhu, Y. Wang, and Y. Zhang, *Recent advances of loose nanofiltration membranes for dye/salt separation.* Separation and Purification Technology, 2022. **285**: p. 120228.
16. Zhang, Z., K. Fan, Y. Liu, and S. Xia, *A review on polyester and polyester-amide thin film composite nanofiltration membranes: Synthesis, characteristics and applications.* Science of The Total Environment, 2023. **858**: p. 159922.
17. Golpour, M. and M. Pakizeh, *Preparation and characterization of new PA-MOF/PPSU-GO membrane for the separation of KHI from water.* Chemical Engineering Journal, 2018. **345**: p. 221-232.
18. Ji, C., S. Xue, Y.-J. Tang, X.-H. Ma, and Z.-L. Xu, *Polyamide membranes with net-like nanostructures induced by different charged mofs for elevated nanofiltration.* ACS Applied Polymer Materials, 2019. **2**(2): p. 585-593.
19. Golpour, M. and M. Pakizeh, *Development of a new nanofiltration membrane for removal of kinetic hydrate inhibitor from water.* Separation and Purification Technology, 2017. **183**: p. 237-248.
20. Liu, S., C. Wu, W.-S. Hung, X. Lu, and K.-R. Lee, *One-step constructed ultrathin Janus polyamide nanofilms with opposite charges for highly efficient nanofiltration.* Journal of Materials Chemistry A, 2017. **5**(44): p. 22988-22996.
21. Tan, Z., S. Chen, X. Peng, L. Zhang, and C. Gao, *Polyamide membranes with nanoscale Turing structures for water purification.* Science, 2018. **360**(6388): p. 518-521.
22. Ma, X.-H., Z.-K. Yao, Z. Yang, H. Guo, Z.-L. Xu, C.Y. Tang, and M. Elimelech, *Nanofoaming of polyamide desalination membranes to tune permeability and selectivity.* Environmental Science & Technology Letters, 2018. **5**(2): p. 123-130.
23. Chowdhury, M.R., J. Steffes, B.D. Huey, and J.R. McCutcheon, *3D printed polyamide membranes for desalination.* Science, 2018. **361**(6403): p. 682-686.
24. Han, S., W. You, S. Lv, C. Du, X. Zhang, E. Zhang, J. Zhu, and Y. Zhang, *Ionic liquid modified COF nanosheet interlayered polyamide membranes for elevated nanofiltration performance.* Desalination, 2023. **548**: p. 116300.
25. Xie, T., F. Li, K. Chen, S. Zhao, Y. Chen, H. Sun, P. Li, and Q.J. Niu, *Fabrication of novel thin-film nanocomposite polyamide membrane by the interlayer approach: A review*. Desalination, 2023. **554**: p. 116509.
26. Lu, J., Y. Qin, Q. Zhang, Y. Wu, J. Cui, C. Li, L. Wang, and Y. Yan, *Multilayered ion-imprinted membranes with high selectivity towards Li+ based on the synergistic effect of 12-crown-4 and polyether sulfone.* Applied Surface Science, 2018. **427**: p. 931-941.
27. Zhu, J., L. Qin, A. Uliana, J. Hou, J. Wang, Y. Zhang, X. Li, S. Yuan, J. Li, and M. Tian, *Elevated performance of thin film nanocomposite membranes enabled by modified hydrophilic MOFs for nanofiltration.* ACS applied materials & interfaces, 2017. **9**(2): p. 1975-1986.
28. Yin, J., G. Zhu, and B. Deng, *Graphene oxide (GO) enhanced polyamide (PA) thin-film nanocomposite (TFN) membrane for water purification.* Desalination, 2016. **379**: p. 93-101.
29. Son, M., H. Park, L. Liu, H. Choi, J.H. Kim, and H. Choi, *Thin-film nanocomposite membrane with CNT positioning in support layer for energy harvesting from saline water.* Chemical Engineering Journal, 2016. **284**: p. 68-77.
30. Dong, L.-x., X.-c. Huang, Z. Wang, Z. Yang, X.-m. Wang, and C.Y. Tang, *A thin-film nanocomposite nanofiltration membrane prepared on a support with in situ embedded zeolite nanoparticles.* Separation and Purification Technology, 2016. **166**: p. 230-239.
31. Bojnourd, F.M. and M. Pakizeh, *Preparation and characterization of a nanoclay/PVA/PSf nanocomposite membrane for removal of pharmaceuticals from water.* Applied Clay Science, 2018. **162**: p. 326-338.

32. Sorribas, S., P. Gorgojo, C. Téllez, J. Coronas, and A.G. Livingston, *High flux thin film nanocomposite membranes based on metal–organic frameworks for organic solvent nanofiltration.* Journal of the American Chemical Society, 2013. **135**(40): p. 15201-15208.
33. Abdollahzadeh, M., M. Chai, E. Hosseini, M. Zakertabrizi, M. Mohammad, H. Ahmadi, J. Hou, S. Lim, A. Habibnejad Korayem, and V. Chen, *Designing Angstrom‐Scale Asymmetric MOF‐on‐MOF Cavities for High Monovalent Ion Selectivity.* Advanced Materials, 2022. **34**(9): p. 2107878.
34. Xiao, H., M. Chai, M. Abdollahzadeh, H. Ahmadi, V. Chen, D.B. Gore, M. Asadnia, and A. Razmjou, *A lithium ion selective membrane synthesized from a double layered Zrbased metalorganic framework (MOF-on-MOF) thin film.* Desalination, 2022. **532**: p. 115733.
35. Zhao, J., R. Fan, S. Xiang, J. Hu, and X. Zheng, *Preparation and Lithium-Ion Separation Property of ZIF-8 Membrane with Excellent Flexibility.* Membranes, 2023. **13**(5): p. 500.
36. Park, S.H., K. Kim, J.H. Lim, and S.J. Lee, *Selective lithium and magnesium adsorption by phosphonate metal-organic framework-incorporated alginate hydrogel inspired from lithium adsorption characteristics of brown algae.* Separation and Purification Technology, 2019. **212**: p. 611-618.
37. Mohammad, M., M. Lisiecki, K. Liang, A. Razmjou, and V. Chen, *Metal-Phenolic network and metal-organic framework composite membrane for lithium ion extraction.* Applied Materials Today, 2020. **21**: p. 100884.
38. Raggam, S., M. Mohammad, Y. Choo, G. Naidu, M. Zargar, H.K. Shon, and A. Razmjou, *Advances in metal organic framework (MOF)–Based membranes and adsorbents for lithium-ion extraction.* Separation and Purification Technology, 2023. **307**: p. 122628.
39. Liu, Y., R. Zhu, C. Srinivasakannan, T. Li, S. Li, S. Yin, and L. Zhang, *Application of Nanofiltration Membrane Based on Metal-Organic Frameworks (MOFs) in the Separation of Magnesium and Lithium from Salt Lakes.* Separations, 2022. **9**(11): p. 344.
40. Ma, D., S.B. Peh, G. Han, and S.B. Chen, *Thin-film nanocomposite (TFN) membranes incorporated with super-hydrophilic metal–organic framework (MOF) UiO-66: toward enhancement of water flux and salt rejection.* ACS Applied Materials & Interfaces, 2017. **9**(8): p. 7523-7534.
41. Xiao, S., X. Huo, Y. Tong, C. Cheng, S. Yu, and X. Tan, *Improvement of thin-film nanocomposite (TFN) membrane performance by CAU-1 with low charge and small size.* Separation and Purification Technology, 2021. **274**: p. 118467.
42. Férey, G., C. Mellot-Draznieks, C. Serre, F. Millange, J. Dutour, S. Surblé, and I. Margiolaki, *A chromium terephthalate-based solid with unusually large pore volumes and surface area.* Science, 2005. **309**(5743): p. 2040-2042.
43. Wang, C., X. Liu, N.K. Demir, J.P. Chen, and K. Li, *Applications of water stable metal–organic frameworks.* Chemical Society Reviews, 2016. **45**(18): p. 5107-5134.
44. Xiao, H., M. Chai, A. Hosseini, A.H. Korayem, M. Abdollahzadeh, H. Ahmadi, V. Chen, D.B. Gore, M. Asadnia, and A. Razmjou, *UiO-66-(COONa) 2 membrane with programmable ionic channels for lithium ion-selective transport.* Journal of Membrane Science, 2023. **670**: p. 121312.
45. Zhao, Y., M. Wu, Y. Guo, N. Mamrol, X. Yang, C. Gao, and B. Van der Bruggen, *Metal-organic framework based membranes for selective separation of target ions.* Journal of Membrane Science, 2021: p. 119407.
46. Song, N., Y. Sun, X. Xie, D. Wang, F. Shao, L. Yu, and L. Dong, *Doping MIL-101 (Cr)@ GO in polyamide nanocomposite membranes with improved water flux.* Desalination, 2020. **492**: p. 114601.
47. Polyukhov, D.M., A.S. Poryvaev, S.A. Gromilov, and M.V. Fedin, *Precise measurement and controlled tuning of effective window sizes in ZIF-8 framework for efficient separation of xylenes.* Nano letters, 2019. **19**(9): p. 6506-6510.

48. Sampaio, A.M., A.R. Nabais, L.C. Tomé, and L.A. Neves, *Impact of MOF-5 on pyrrolidinium-based poly (ionic liquid)/ionic liquid membranes for biogas upgrading.* Industrial & Engineering Chemistry Research, 2019. **59**(1): p. 308-317.
49. Gupta, K.M., Y. Chen, Z. Hu, and J. Jiang, *Metal–organic framework supported ionic liquid membranes for CO 2 capture: anion effects.* Physical Chemistry Chemical Physics, 2012. **14**(16): p. 5785-5794.
50. Park, S. and H.-K. Jeong, *Highly H 2 O permeable ionic liquid encapsulated metal–organic framework membranes for energy-efficient air-dehumidification.* Journal of Materials Chemistry A, 2020. **8**(44): p. 23645-23653.
51. Ng, Z.C., W.J. Lau, and A.F. Ismail, *GO/PVA-integrated TFN RO membrane: Exploring the effect of orientation switching between PA and GO/PVA and evaluating the GO loading impact.* Desalination, 2020. **496**: p. 114538.
52. Vital, B., J. Bartacek, J. Ortega-Bravo, and D. Jeison, *Treatment of acid mine drainage by forward osmosis: Heavy metal rejection and reverse flux of draw solution constituents.* Chemical Engineering Journal, 2018. **332**: p. 85-91.
53. Ni, T. and Q. Ge, *Highly hydrophilic thin-film composition forward osmosis (FO) membranes functionalized with aniline sulfonate/bisulfonate for desalination.* Journal of Membrane Science, 2018. **564**: p. 732-741.
54. Khoo, Y.S., W.J. Lau, Y.Y. Liang, M. Karaman, M. Gürsoy, and A.F. Ismail, *Eco-friendly surface modification approach to develop thin film nanocomposite membrane with improved desalination and antifouling properties.* Journal of advanced research, 2022. **36**: p. 39-49.
55. Vu, T.A., G.H. Le, C.D. Dao, L.Q. Dang, K.T. Nguyen, P.T. Dang, H.T. Tran, Q.T. Duong, T.V. Nguyen, and G.D. Lee, *Isomorphous substitution of Cr by Fe in MIL-101 framework and its application as a novel heterogeneous photo-Fenton catalyst for reactive dye degradation.* Rsc Advances, 2014. **4**(78): p. 41185-41194.
56. Niknam, E., F. Panahi, F. Daneshgar, F. Bahrami, and A. Khalafi-Nezhad, *Metal–organic framework MIL-101 (Cr) as an efficient heterogeneous catalyst for clean synthesis of benzoazoles.* ACS omega, 2018. **3**(12): p. 17135-17144.
57. Huang, X., Q. Hu, L. Gao, Q. Hao, P. Wang, and D. Qin, *Adsorption characteristics of metal–organic framework MIL-101 (Cr) towards sulfamethoxazole and its persulfate oxidation regeneration.* RSC advances, 2018. **8**(49): p. 27623-27630.
58. Jaleh, B., N. Gavary, P. Fakhri, N. Muensit, and S.M. Taheri, *Characteristics of PVDF membranes irradiated by electron beam.* Membranes, 2015. **5**(1): p. 1-10.
59. Bai, H., X. Wang, Y. Zhou, and L. Zhang, *Preparation and characterization of poly (vinylidene fluoride) composite membranes blended with nano-crystalline cellulose.* Progress in Natural Science: Materials International, 2012. **22**(3): p. 250-257.
60. Mohammadi Ghaleni, M., A. Al Balushi, S. Kaviani, E. Tavakoli, M. Bavarian, and S. Nejati, *Fabrication of Janus membranes for desalination of oil-contaminated saline water.* ACS applied materials & interfaces, 2018. **10**(51): p. 44871-44879.
61. Kaspar, P., D. Sobola, K. Částková, R. Dallaev, E. Šťastná, P. Sedlák, A. Knápek, T. Trčka, and V. Holcman, *Case study of polyvinylidene fluoride doping by carbon nanotubes.* Materials, 2021. **14**(6): p. 1428.
62. Gao, X., P. Li, Z. Gu, Q. Xiao, S. Yu, and L.a. Hou, *Preparation of poly (piperazine-amide) nanofilms with micro-wrinkled surface via nanoparticle-templated interfacial polymerization: Performance and mechanism.* Journal of Membrane Science, 2021. **638**: p. 119711.
63. Istirokhatun, T., Y. Lin, Q. Shen, K. Guan, S. Wang, and H. Matsuyama, *Ag-based nanocapsule-regulated interfacial polymerization Enables synchronous nanostructure towards high-performance nanofiltration membrane for sustainable water remediation.* Journal of Membrane Science, 2022. **645**: p. 120196.

64. He, M., L. Wang, Y. Lv, X. Wang, J. Zhu, Y. Zhang, and T. Liu, *Novel polydopamine/metal organic framework thin film nanocomposite forward osmosis membrane for salt rejection and heavy metal removal.* Chemical Engineering Journal, 2020. **389**: p. 124452.
65. Vrijenhoek, E.M., S. Hong, and M. Elimelech, *Influence of membrane surface properties on initial rate of colloidal fouling of reverse osmosis and nanofiltration membranes.* Journal of membrane science, 2001. **188**(1): p. 115-128.
66. Bi, R., Q. Zhang, R. Zhang, Y. Su, and Z. Jiang, *Thin film nanocomposite membranes incorporated with graphene quantum dots for high flux and antifouling property.* Journal of Membrane Science, 2018. **553**: p. 17-24.
67. Guo, F., J. Miao, L. Xu, Q. Zhou, and T. Deng, *Conductive thin-film nanocomposite nanofiltration membrane comprising N-doped graphene quantum dots with relieved concentration polarization for sulfate separation from high-salinity solution.* Desalination, 2023. **555**: p. 116526.
68. Mousavi, S.R., M. Asghari, N.M. Mahmoodi, and I. Salahshoori, *Water decolorization and antifouling melioration of a novel PEBA1657/PES TFC membrane using chitosan-decorated graphene oxide fillers.* Journal of Environmental Chemical Engineering, 2023. **11**(3): p. 109955.
69. Wang, J., Z. Yue, and J. Economy, *Solvent resistant hydrolyzed polyacrylonitrile membranes.* Separation Science and Technology, 2009. **44**(12): p. 2827-2839.
70. Zhao, Y., Y. Liu, C. Wang, E. Ortega, X. Wang, Y.F. Xie, J. Shen, C. Gao, and B. Van der Bruggen, *Electric field-based ionic control of selective separation layers.* Journal of Materials Chemistry A, 2020. **8**(8): p. 4244-4251.
71. Campbell, J., J.D.S. Burgal, G. Szekely, R. Davies, D.C. Braddock, and A. Livingston, *Hybrid polymer/MOF membranes for Organic Solvent Nanofiltration (OSN): Chemical modification and the quest for perfection.* Journal of Membrane Science, 2016. **503**: p. 166-176.
72. Zheng, J., X. Zhang, G. Li, G. Fei, P. Jin, Y. Liu, C. Wouters, G. Meir, Y. Li, and B. Van der Bruggen, *Selective removal of heavy metals from saline water by nanofiltration.* Desalination, 2022. **525**: p. 115380.
73. Wu, Y., R. Lin, F. Ma, W. Xing, and J. Pan, *Three-dimensional macroporous wood-based selective separation membranes decorated with well-designed Nd (III)-imprinted domains: A high-efficiency recovery system for rare earth element.* Journal of Colloid and Interface Science, 2021. **587**: p. 703-714.
74. Bi, Q. and S. Xu, *Separation of magnesium and lithium from brine with high Mg2+/Li+ ratio by a two-stage nanofiltration process.* Desalination and Water Treatment, 2018. **129**: p. 94-100.
75. Kumar, R., C. Liu, G.-S. Ha, Y.-K. Park, M.A. Khan, M. Jang, S.-H. Kim, M.A. Amin, A. Gacem, and B.-H. Jeon, *Downstream recovery of Li and value-added metals (Ni, Co, and Mn) from leach liquor of spent lithium-ion batteries using a membrane-integrated hybrid system.* Chemical Engineering Journal, 2022. **447**: p. 137507.
76. Xu, Q., F. Yang, X. Zhang, J.R. Li, J.F. Chen, and S. Zhang, *Combining Ionic Liquids and Sodium Salts into Metal‐Organic Framework for High‐Performance Ionic Conduction.* ChemElectroChem, 2020. **7**(1): p. 183-190.
77. Zhang, M., A.-M. Zhang, X.-X. Wang, Q. Huang, X. Zhu, X.-L. Wang, L.-Z. Dong, S.-L. Li, and Y.-Q. Lan, *Encapsulating ionic liquids into POM-based MOFs to improve their conductivity for superior lithium storage.* Journal of Materials Chemistry A, 2018. **6**(18): p. 8735-8741.
78. Ghanbari, M., D. Emadzadeh, W. Lau, S. Lai, T. Matsuura, and A. Ismail, *Synthesis and characterization of novel thin film nanocomposite (TFN) membranes embedded with halloysite nanotubes (HNTs) for water desalination.* Desalination, 2015. **358**: p. 33-41.
79. Morra, M., *On the molecular basis of fouling resistance.* Journal of Biomaterials Science, Polymer Edition, 2000. **11**(6): p. 547-569.

80. Shi, W., X. Liu, C. Ye, X. Cao, C. Gao, and J. Shen, *Efficient lithium extraction by membrane capacitive deionization incorporated with monovalent selective cation exchange membrane.* Separation and Purification Technology, 2019. **210**: p. 885-890.
81. Zhao, L.-M., Q.-B. Chen, Z.-Y. Ji, J. Liu, Y.-Y. Zhao, X.-F. Guo, and J.-S. Yuan, *Separating and recovering lithium from brines using selective-electrodialysis: Sensitivity to temperature.* Chemical Engineering Research and Design, 2018. **140**: p. 116-127.
82. Cerda, A., M. Quilaqueo, L. Barros, G. Seriche, M. Gim-Krumm, S. Santoro, A.H. Avci, J. Romero, E. Curcio, and H. Estay, *Recovering water from lithium-rich brines by a fractionation process based on membrane distillation-crystallization.* Journal of Water Process Engineering, 2021. **41**: p. 102063.
83. Zhao, K., B. Tong, X. Yu, Y. Guo, Y. Xie, and T. Deng, *Synthesis of porous fiber-supported lithium ion-sieve adsorbent for lithium recovery from geothermal water.* Chemical Engineering Journal, 2022. **430**: p. 131423.
84. Yang, J., G. Qu, C. Liu, S. Zhou, B. Li, and Y. Wei, *An effective lithium ion-imprinted membrane containing 12-crown ether-4 for selective recovery of lithium.* Chemical Engineering Research and Design, 2022. **184**: p. 639-650.
85. Wang, L., D. Rehman, P.-F. Sun, A. Deshmukh, L. Zhang, Q. Han, Z. Yang, Z. Wang, H.-D. Park, and J.H. Lienhard, *Novel positively charged metal-coordinated nanofiltration membrane for lithium recovery.* ACS Applied Materials & Interfaces, 2021. **13**(14): p. 16906-16915.
86. Gan, Q., C. Wu, L. Long, L.E. Peng, Z. Yang, H. Guo, and C.Y. Tang, *Does surface roughness necessarily increase the fouling propensity of polyamide reverse osmosis membranes by humic acid?* Environmental Science & Technology, 2023. **57**(6): p. 2548-2556.
87. Aljubran, M.A., Z. Ali, Y. Wang, E. Alonso, T. Puspasari, K. Cherviakouski, and I. Pinnau, *Highly efficient size-sieving-based removal of arsenic (III) via defect-free interfacially-polymerized polyamide thin-film composite membranes.* Journal of Membrane Science, 2022. **652**: p. 120477.
88. Mills, R., K.C. Baldridge, M. Bernard, and D. Bhattacharyya, *Recent advances in responsive membrane functionalization approaches and applications.* Separation Science and Technology, 2023. **58**(6): p. 1202-1236.
89. Shao, D.-D., R. Fang, L. Wang, Y. Wang, X.-L. Cao, M.-L. Liu, X. Li, and S.-P. Sun, *Dispersant promotes mild formation of aminated-carbon quantum dots nanofiltration membranes for high-efficient resource recovery.* Separation and Purification Technology, 2023. **316**: p. 123759.
90. Zante, G., A. Masmoudi, R. Barillon, D. Trébouet, and M. Boltoeva, *Separation of lithium, cobalt and nickel from spent lithium-ion batteries using TBP and imidazolium-based ionic liquids.* Journal of Industrial and Engineering Chemistry, 2020. **82**: p. 269-277.
91. Zante, G., M. Boltoeva, A. Masmoudi, R. Barillon, and D. Trebouet, *Lithium extraction from complex aqueous solutions using supported ionic liquid membranes.* Journal of Membrane Science, 2019. **580**: p. 62-76.
92. Hou, J., H. Zhang, A.W. Thornton, A.J. Hill, H. Wang, and K. Konstas, *Lithium extraction by emerging metal‐organic framework‐based membranes.* Advanced functional materials, 2021. **31**(46): p. 2105991.